Master Thesis

Nanostructure of bone in healthy and tumorous tissue

carried out for the purpose of obtaining the degree of Master of Science,
submitted at TU Wien, Faculty of Mechanical and Industrial Engineering, by

Benjamin Zanghellini

Matr.Nr.: 01040491

Alser Straße 30/4/58

1090 Vienna

Austria

under the supervision of

Univ.Prof. Mag. Dr.rer.nat. Lichtenegger

Institute of Physics and Materials Science (IPM)

& under the co-supervision of

Dr. Tilman Grünewald

ESRF Grenoble

_____

B. Zanghellini   H. Lichtenegger

Nanostructure of bone in healthy and tumorous tissue

Benjamin Zanghellini

Mat.Nr.: 01040491

Declaration of Authorship

I confirm, that going to press of this thesis needs the confirmation of the examination committee.

Affidavit

I declare in lieu of oath, that I wrote this thesis and performed the associated research myself, using only literature cited in this volume. If text passages from sources are listed literally, they are marked as such.
I confirm that this work is original and has not been submitted elsewhere for any examination, nor is it currently under consideration for a thesis elsewhere.

Vienna, December 2017

Abstract

Over the last centuries, the standard of health of our society has improved immensely. Consequently, also the field of research in cancer expanded by the ability of using new techniques to investigate diseases like, for instance, bone cancer. Through that, it is more important than ever to investigate all aspects of these malignant mechanisms. Although the mechanisms of osteosarcomas are known to a high extent, some malfunctions have not been fully explored yet. Up to now, it is still not clear, whether and to what extent this sort of cancer has an influence on the nanostructure of bone. The aim of this thesis was to respond to this question. This was accomplished by the method of small angle x-ray scattering (SAXS), and the method of backscattered electron imaging (BEI). In the course of this thesis, healthy and assumed to be tumorous bone tissue samples were examined. Through the method of SAXS it was possible to investigate the nanostructure of bone, to be more precise, it provides insights into the thickness of the mineral platelets and the orientation of the mineral/collagen composite. In addition to that, the samples were also probed in the scanning electron microscope SEM. This method should complement the SAXS results of the tumorous bone tissue parts by analyzing the bone mineral density, which is assumed to be decreased in osteosarcomas. In this thesis, the following results based on the applied methods are discussed in detail:

- The differences in the thickness of the mineral platelets in healthy and tumorous bone tissue
- The changes in the degree of orientation of the collagen fibrils when suffering from osteosarcoma
- The determination of the bone mineral density in the different samples

Kurzbeschreibung

Im Laufe der letzten Jahrzehnte haben sich die Gesundheitsstandards und die Lebenserwartung unserer Gesellschaft rasant weiterentwickelt und verbessert. Dadurch erweiterten sich auch die Forschungsbereiche im Sektor der Krebsforschung und es ist nun möglich, Erkrankungen, wie Knochenkrebs, mittels neuartiger Entwicklungen zu untersuchen. Im Zuge dessen, wird es immer wichtiger alle Aspekte und Mechanismen solcher Erkrankungen zu untersuchen und zu verstehen. Obwohl viele Merkmale des Osteosarkoms bereits bekannt sind, gibt es immer noch Eigenschaften die nicht völlig geklärt sind. Bis heute ist es nicht völlig klar, welchen Einfluss diese Art von Krebs auf die Nanostruktur von Knochen hat. Ziel dieser Masterarbeit war es, zu versuchen, diese Fragestellung zu klären. Dies wurde erreicht unter der Verwendung der Methode der Kleinwinkelstreuung (SAXS) und der bildgebenden Elektronenrückstreuung (BEI). Im Zuge dieser Masterarbeit wurden gesunde und vermutete tumoröse Knochenbereiche untersucht. Mittels SAXS war es möglich die Nanostruktur des Kochens zu untersuchen. Im Detail erhält man dadurch Information über die Dicke der Mineralplättchen und die Orientierung der Kollagen Fibrille. Zusätzlich wurden die Proben auch im SEM untersucht. Diese Methode sollte dazu dienen, die Tumorbereiche mittels der Bestimmung der Mineraldichte zu charakterisieren und dadurch die SAXS Ergebnisse zu ergänzen. Dies ist grundsätzlich möglich, da die Mineraldichte im Knochen in Bereichen des Osteosarkoms reduziert ist. In dieser Masterarbeit wurden folgende Resultate, basierend auf den angewendeten Methoden, im Detail diskutiert und präsentiert:

- Die Unterschiede der Dicke der Mineralplättchen in gesundem und tumorösen Knochengewebe
- Die Änderung des Grades der Orientierung der Kollagen Fibrille
- Die Bestimmung der Knochendichte der unterschiedlichen Proben

Content

III. Results   43

List of abbreviations

Å	Angström
BEI	Backscattered electron imaging
C	Carbon
MgF^2	Magnesium fluoride
HA	Hydroxyapatite
mA	Milli-ampere
mm	Millimeters
μm	Micrometers
nm	Nanometers
NO1	Normal bone tissue region 1
NO2	Normal bone tissue region 2
OPG	osteoprotegerin
OS	osteosarcoma
PMMA	polymethylacrylate
PTH	Parathyroid hormone
qBEI	Quantitative backscattered electron imaging
RANK	Receptor activator of nuclear factor κB
RANKL	Receptor activator of nuclear factor κB ligand
RR1	Resection margin sample region 1 cortical bone
RR2	Resection margin sample region 2 cortical bone
RR1trab	Resection margin sample region 1 trabecular bone
RR2trab	Resection margin sample region 2 trabecular bone
*sample*_norm	Healthy bone tissue area within one of the samples stated above
*sample*_tu	Tumorous bone tissue area within one of the samples stated above
SAXS	Small angle x-ray scattering
SEM	Scanning electron microscope
TGF	Transforming growth factors
TU1	Tumorous bone tissue sample region 1
TU3	Tumorous bone tissue sample region 3
UG1	Crossing tissue sample region 1
UG1bottom	Crossing tissue sample bottom region

Introduction

Osteosarcoma is the most common primary bone cancer. Due to the steady increase of our life expectancy, cancer is a disease, which occurs more and more frequently. Therefore, the investigations of the mechanisms of these diseases are getting even more important. People who are suffering from such diseases are confronted with high restrictions of their life quality, leading in the most tragic cases finally, even nowadays, to death. Thus, it is necessary to understand all mechanisms in order to be able to develop more appropriate curing methods.

Bone can be seen as a biomaterial with a highly hierarchical structure and lots of important and sufficient tasks in our body. Therefore, in this thesis, the focus was also on describing these characteristics to gain a small insight in the composition and the function of our skeleton.

When cancer infests bones, abnormal functions arise, which influence and change the normal processes of bones and destroy healthy tissue parts. Through the course of this thesis bone samples of a special form of bone cancer, named osteosarcoma, were available and investigated.

Although bone cancer, and especially osteosarcoma, are characterized very well, it is still not known if the nanostructure of bones is changed. In this thesis it was attempted to investigate and visualize nanostructure changes by applying the method of small angle x-ray scattering and backscattered electron imaging. SAXS is a non-destructive method and it can be used, through the scattering of x-rays on the samples at small angles, to analyze structure properties, such as the thickness of the mineral platelets and the orientation of collagen fibrils, of the specimen.

I. Theory

1. Bone

Bones can be seen as the primary unit of our skeleton, which is built up by 206 of them in different shapes and sizes such as long bones, short bones or sesamoid bones. Besides the kinematic aspects bone provides other important functions. It acts as a mineral reservoir and stores calcium and phosphor, protects our vital organs like the heart or the lungs and is also the place of haematopoiesis.

Over the last decades, more and more focus was laid on the characterization, identification and treatment of bone diseases, but the full mechanisms of some malfunctions are still unknown. To achieve these goals, it is essential to understand the properties, structures and mechanisms of bones and how they change in case of being influenced of a disease.

1.1 Hierarchical structure and composition

Bone is a highly hierarchically structured, transverse isotropic material which consists of organic and inorganic components (about 10-20% water; dry mass: 60-70% mineral constituents and 10-20% collagen fibres). The main organic material is type-I collagen with about 90-95%. Further, organic and noncollagenous proteins are found in bone such as osteocalcin, osteopontin or osteonectin. The main inorganic material is the mineral hydroxyapatite, other inorganic components are magnesium or sodium-based salts (Mottaghitalab et al., 2015, p. 113).

Moreover, bone can be divided into different organized levels down to the nanometre level (see figure 1.1 according to (Rho, Kuhn-Spearing, & Zioupos, 1998, p. 92):

- The macrostructure, composed of bones of different shapes, consists of cancellous and trabecular bone
- The micro- and submicrostructure, which is in a range of 10 to 500 micrometres; on this level osteons, the harversian canal and single trabeculae, on the submicrostructure-level (1 to 10 micrometres) the lamellae are found;
- The nano- and subnanostructure is situated in a region of a few hundred nanometres up to 1 micrometres, with the subnanostructure starting below the lower threshold; these are the levels of (i) mineralized collagen fibres and fibrils

and (ii) the molecular structures e.g. of collagen, mineral, or other non-collagenous organic proteins; (Rho et al., 1998, p. 92).
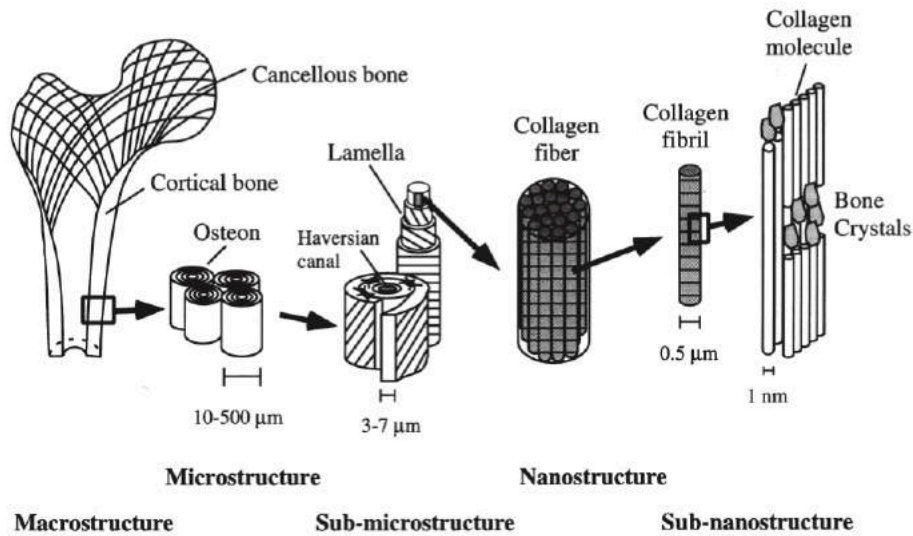

figure 1.1 bone and its hierarchical structure: displayed levels from micro- to subnanostructure; adapted from (Rho et al., 1998, p. 92)

1.1.1 The macrostructure

On this level, bones can be distinguished based on their different shapes, which are long, short, sesamoid, flat and irregular bones. In addition to that, their mechanical properties, depending on the bone's function and optimized for it, can be detected on this hierarchical structure. Considering for instance the mechanically most relevant bones: long bones must withstand different modes of loading in contrast to the vertebra, which represents an irregular bone. Thus, for instance the femur has a good counteraction to bending and buckling, whilst a vertebra resists loads mostly in compression (Fratzl & Weinkamer, 2007, p. 1270). Further, the macrostructure of bone can be divided into two categories, cortical, which forms the outer shell, and cancellous bone which is found in the inner parts of the bone (see figure 1.2). These two show different microstructures, with trabecular bone is formed by single trabeculae and cortical bone is made up by osteons, which is described in detail later on. (Georgiadis, Muller, & Schneider, 2016, p. 1)

Another difference between these two types is the degree of porosity, but the basic bone material composition is identical. Through the different degree of porosity also the mechanical properties of cancellous and cortical bone are different. The porosity of cortical bone is in a range of 5-10% in contrast to 50-95% of trabecular

bone, so cortical bone is much stiffer than trabecular bone. The average strength of human compact bone in longitudinal compression is 105 MPa, in transversal compression 131 MPa and in longitudinal tension 53 MPa but these values vary somewhat among individuals and different bones in the same individual (Mottaghitalab et al., 2015, p. 113).
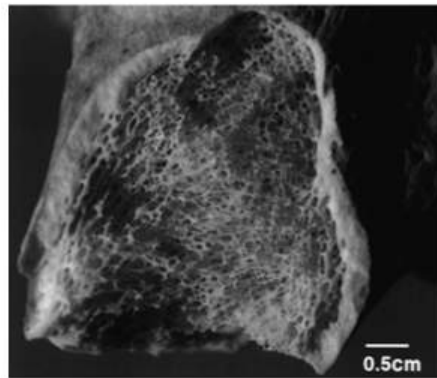
figure 1.2 cortical vs trabecular bone areas; adapted from (Olszta et al., 2007)

1.1.2 The microstructure

At this level structures like osteons or single trabeculae are found (see figure 1.3). As described before cortical bone is considerably denser, the porosity of 5-10% results from the blood vessels and nerves which are also located there and supply the bone. The canal where these are travelling through is then the so-called Harversian canal (Fratzl & Weinkamer, 2007, pp. 1270-1271).

The vessels and nerves are surrounded by compact bone material in the form of concentric layers (with up to 20 layers); this formation is called osteon or harversian system, has a diameter of 200 to 250 µm and the order is almost parallel to the long axis of the bone (Rho et al., 1998, pp. 94-96). On the sub-microstructure level one single concentric layer is referred to as lamella which is formed by mineralized collagen fibril bundles with a thickness of 3 to 7 µm and is embedded in an extrafibrillar matrix (Schrof, Varga, Galvis, Raum, & Masic, 2014, p. 266). Both, cortical and cancellous bone are formed by lamellae, with the difference that no Harversian canals are formed in trabecular bone by lamellae (Rho et al., 1998, pp. 94-96).

figure 1.3 left: harversian system, right: single trabeculae, both images obtained by back-scattered electron imaging; adapted from (Fratzl, Gupta, Paschalis, & Roschger, 2004)
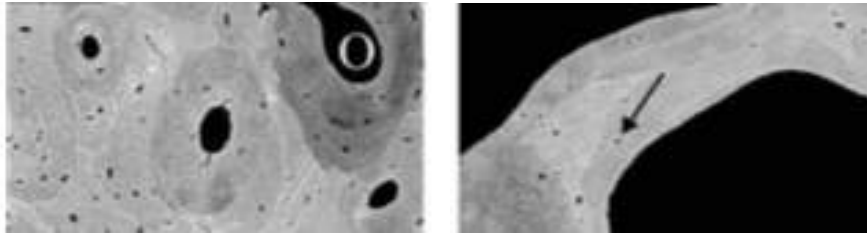
Cancellous bone has a higher porosity and can be seen as a foam-like scaffold of trabeculae (see figure 1.4). Considering the thickness, it can be said that a single trabecula is in the range of about 200 micrometers, while the orientation depends strongly on how the bone is loaded in this area. In the right image of figure 1.3 the arrow marks one of the osteocytes, which are the residuals of the osteoblasts, and are surrounded completely by bone material. Further, the trabecular matrix is surrounded by bone marrow which contains blood and is amongst other things also the place of hematopoiesis (note: red bone marrow) (Fratzl & Weinkamer, 2007, pp. 1272-1273).
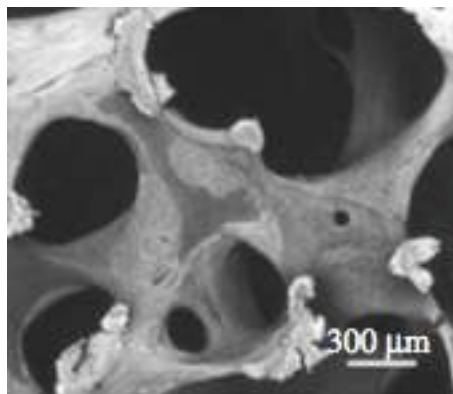
figure 1.4 Trabecular bone, which is formed of network of trabeculae; adapted from (Georgiadis et al., 2016)

1.1.3 The nanostructure

At the scale of a few hundred nanometres up to one micrometre bone can be seen as a composite of collagen fibres, which are formed by collagen fibrils, mainly type-I collagen, and are infiltrated by mineral particles, more precisely carbonated hydroxyapatite (Fratzl & Weinkamer, 2007, p. 1273).

On the hierarchical level of sub-nanostructures, the collagen molecules, that are the basic building block of the collagen fibrils, the mineral crystals and non-collagenous organic proteins are found. The primary structure of collagen is formed by the repeating the amino acid sequences -(Gly-X-Y-)$_n$-, Gly, X and Y represent

glycine, proline and hydroxyproline residues. Due to that, the protein can arrange in triple helical structures which are called tropocollagen molecules. A single collagen molecule is about 300 nm long and 1.5 nm thick due to secondary bonding interactions. Due to the quarter staggered array, this arrangement leads to gap and overlap zones (see figure 1.5) (Olszta et al., 2007, pp. 81-82).

collagen
fibril

→ ← 1.23 nm

collagen
molecules

hole zone

300 nm

40 nm
27 nm

protein
triple
helix

bone mineral
crystal
50 x 25 x 3 nm
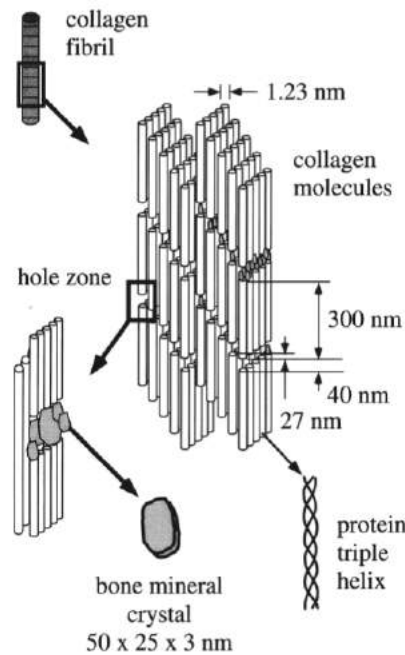
figure 1.5 alignment of collagen fibres and mineral particles: mineral platelets fill the cap zones of the staggered arrangement of the collagen molecules; adapted from (Rho et al., 1998)

To be more precise, the staggered molecules are arranged in a distance of 67 nm in between, as a consequence this generates overlap zones of 32 nm and gap zones of 35 nm length. The mineral particles fill up these zones and are mainly flat plates. These crystals are found every 67 nm in a fibril. Moreover, the mineral particles are ordered parallel to the long axis of the collagen molecules. (see figure 1.6) (Fratzl & Weinkamer, 2007, pp. 1273-1274).

Most of the recent studies of the geometry of the mineral particles (carried out by TEM and SAXS) showed a plate-like shape of those. (Fratzl et al., 2004, p. 2117)

The dimension of these platelets is in a range of approximately 50 nm in length, 25 nm in width and 3 nm in thickness. (Georgiadis et al., 2016)

Further, measurements in human bone showed that the collagen fibril consist of about 60% gap zones and 40% overlap zones. This leads to the fact that the

maximum mineral content is about 43% in average. These mineralized collagen fibrils can be seen as the basic building blocks of bone (Fratzl et al., 2004, p. 2119).
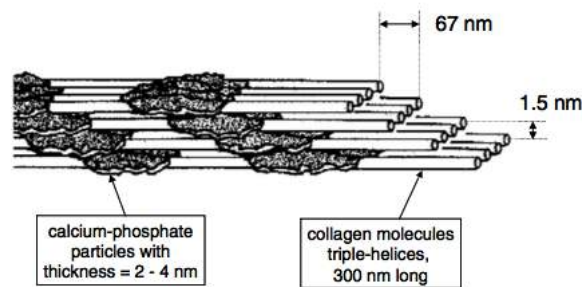

figure 1.6 Arrangement of collagen molecules and mineral cristals in the cap zones; adapted from (Fratzl & Weinkamer, 2007)

1.2 Orientation and role of the collagen-mineral composite in bone

Although the structure of the lamellae has been a target of high interests in research over the recent years, the knowledge of these complex constructions and processes is still limited. It is assumed that the lamellar structure of the cancellous bone (see figure 1.7) can be seen as alternating layers built up of both, ordered and disordered collagen arrays. The majority of the lamellar structure is formed by the ordered collagen fibrils. Further, these ordered arrays are mainly parallel to the boundary layer of the lamellae and are organized in bundles. Two predominant directions of orientation of the whole ordered arrays can be identified: Alignments parallel and oblique to the long axis of the trabecula. Considering the disordered fibrils, they hardly show any preferred orientation. In contrast to the ordered ones, these are also loosely packed. This means that the space between the disordered fibrils is filled with extrafibrillar material, whilst the ordered arrays show a close packaging and through that a minimal amount of the named material (Reznikov, Chase, Brumfeld, Shahar, & Weiner, 2015, p. 191).

The orientation of the lamellae of cortical bone (see figure 1.7) is different from that described before. It is assumed that within one lamella the collagen fibrils show almost a parallel orientation. Further, the orientation changes in adjacent lamellae. (Rho et al., 1998, p. 96) These possible and so-called twisted plywood and oscillating arrangements are investigated in a recent study (Varga et al., 2013, p. 8126).
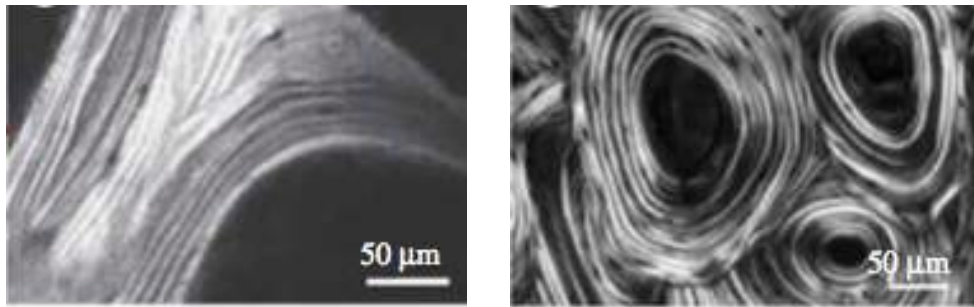
figure 1.7 lamellar structure of trabecular (left) and cortical (right) bone adapted from (Georgiadis et al., 2016)

In a fibril, also the mineral crystals show some orientation: the c-axis of the mineral are mainly parallel to the long axis of the collagen molecules (Rho et al., 1998, p. 97), which is of further importance in the course of this thesis.

Considering the mechanical properties, it can be said that the characteristics depend on the mineral and on the organic components. The mineral contents in the composite contribute mainly to the stiffness of the bone, which means this part influences the yield strain of bone. Considering this fact, this means that bone composites, which show a higher degree of mineralization, are stiffer but also tend to break more easily and faster. On the other hand, the organic phase and especially, due to the high content, collagen type-I, is responsible for tension characteristics. (Fratzl et al., 2004, pp. 2119-2120).

2. Bone tumors

Malignant bone tumors are characterized as sarcomas[1] of cells that are involved in the formation and preservation of bone. This can be either bone, cartilage, endothelial or neuroectodermal cells. Over 90% of all bone tumors are caused by osteosarcomas, Ewing sarcomas or chondrosarcomas (Mascarenhas et al., 1998, p. 99).

The chondrosarcoma is the second most frequent malign bone tumor, only osteosarcomas arise more frequently. It is characterized as a tumor which is thought to be arising from the differentiation of hyaline cartilage. The consequences of this neoplasm can be pathologic calcification and ossification or myxoid alterations. (von Eisenhart-Rothe et al., 2011, pp. 1128-1132).

---

[1] a malign mesenchymal neoplasm

The third of the most frequent sarcomas is the Ewing sarcoma. It is assumed that these tumors arise from neural crest cells (Rajabalian, Hajializadeh, Pooraboli, Jangi-Aghdam, & Badinloo, 2010, p. 331), and can be characterized by the expression of fusion proteins through mutations in the chromosomes (Mahlendorf & Staege, 2013, p. 254). The characteristics of osteosarcomas will be discussed in detail in the following chapters.

2.1 Osteosarcoma

Over the last years the focus was laid on investigating all of the mechanisms of various forms of cancer and to improve the treatments. Major achievements, such as augmentation of the survival rate, could be reached and through that more and more patients can be treated well and are saved from death. Yet, still a major part of malfunctions which are triggered by cancer are still unknown.

First of all, osteosarcomas (OS) are characterized as aggressive malignant osteoblastic cells that are producing immature bone, so-called osteoid (Kansara & Thomas, 2007, p. 1). The highly aggressive behaviour of the osteosarcoma cells leads to a rapid infiltration and devastation of the affected bone tissue (Avnet et al., 2008, p. 1231).

Osteosarcoma is the most widespread type of malignant primary bone cancer people are suffering from and even further the second most common form of cancer that causes death in young people including children. In most of the cases osteosarcoma occurs in the regions of long bones, like the distal femur or the proximal tibia (Yan, Lv, & Guo, 2016, p. 268).

Up to now it is known that in some cases of a diagnosed osteosarcoma risk factors favoured or even led to the arise of the cancer. Such proven factors are the patient´s cancer predisposition syndromes or the suffering from the Paget disease of bone. Another main risk factor to contract an osteosarcoma is given when the patient received therapeutic radiation in the course of another form of cancer (Savage & Mirabello, 2011). Further also some chemical substances, like chromium salts, methylcholanthrene, beryllium oxide or asbestos, can be connected with the occurence of an osteosarcoma (Broadhead, Clark, Myers, Dass, & Choong, 2011, p. 2) . Besides, it has to be said that the majority of osteosarcomas arise without the influence of these risk factors (Savage & Mirabello, 2011). Additionally, one can

find in the appendix aspects of the aetiology of osteosarcomas, which would go beyond the scope in this context.

2.1.1 Pathogenesis

Considering the histological aspects, osteosarcomas can be seen as "a highly cellular tumour composed of pleomorphic spindle-shaped cells capable of producing an osteoid matrix" (Broadhead et al., 2011, p. 1). This matrix represents the immature bone matrix, which is not, or not fully, mineralized. Unfortunately, many, but still not all mechanisms of osteosarcoma are still not known for sure and targets of today's research. In the following the most important ones, that lead to the diseased state, are presented.

2.1.1.1 Genetic aspects

Environmental factors, like for example the mentioned ones above, can have the potential to change or harm the somatic DNA. To avoid a formation of malignant cell lines, the human body reacts with tumour suppressor mechanisms, which are able either to repair the damaged DNA strand or initiate the apoptosis process of the affected cells. Problematically, these suppressor genes can also be affected and even mutate, which has the result of losing the suppressor functions (Broadhead et al., 2011, p. 2).

After a DNA damage the human body counteracts by a higher expression of p53, which is able to inhibit the progress through the cell cycle of the damaged cell or to provoke cell apoptosis. In addition to that, the Rb gene has the ability to regulate the cell cycle progression. It is known, that these two genes are part of the osteosarcoma pathogenesis. Further, is established, that p53 and Rb pathways are blocked in osteosarcomas to a high extent, including the loss of their protective functions (Marina, Gebhardt, Teot, & Gorlick, 2004, pp. 424-425).

Even further, studies showed that both, p53 and Rb, are mutated in 22% of osteosarcomas, additively the Rb gene is obstructed by the transforming growth factor β proteins. Their role in osteosarcomas is annotated in chapter 2.1.3 (Ta, Dass, Choong, & Dunstan, 2009, p. 249).

2.1.1.2 Cell proliferation, metastasis and apoptosis

In general, cancer cells show high resistances to apoptosis, which is the basis of their uncontrolled proliferation (Broadhead, Dass, & Choong, 2009, p. 461). Anoikis can be seen as a special form of apoptosis, it is defined as the programmed cell death when a cell is no longer attached to an extracellular matrix or membrane (Foley et al., 2015, p. 2). It is responsible for the regulation of cell homeostasis in tissues and has a role in tissue remodelling and wound healing. (Strauss, Ng, Mendoza-Naranjo, Whelan, & Sorensen, 2010, p. 629)

This process is of special interest when talking about osteosarcoma cells and their metastases. The spread from cancer cells is a complex process involving various sequences including the separation from the primary site, the invasion through the basement membrane in the blood or lymphatic circulation, the extravasation in an other organ and the proliferation there (see figure 2.1). Since these cells then lack the attachment to the extracellular matrix, they should normally undergo anoikis. In the review of Strauss et al. and Foley et al. it is shown that osteosarcomas have the ability to show resistance to anoikis and to chemotherapy, leading to an anchorage-independent growth, which is essential for the progression of metastasis (Foley et al., 2015, p. 2), of the cancer cells (Strauss et al., 2010, pp. 628-633).
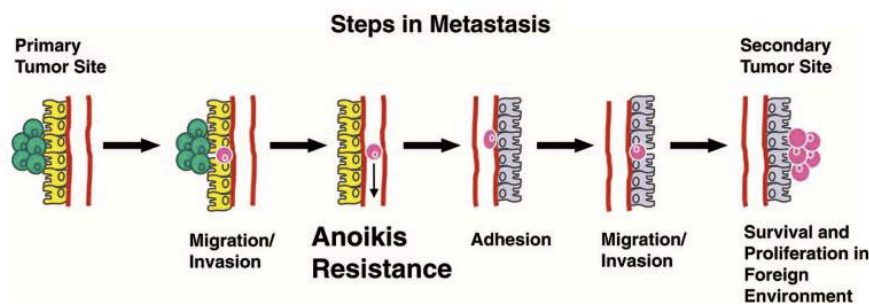

figure 2.1 sequences of metastasis of cancer cells beginning with the invasion of the cancer cells; adapted from (Strauss et al., 2010)

2.1.1.3 Growth factors influencing osteosarcoma cells

It is already known, that the malignant cells possess the ability to unregulated production of growth factors, which causes an expedited proliferation of these cells, amongst others (Broadhead et al., 2011, p. 3).

Considering for example the transforming growth factor β proteins (TGF-β1, -β2 and -β3), it is known that these peptides are responsible for the regulation of the cell growth, the cell differentiation, the cell proliferation and the production of the extracellular matrix, amongst other growth factors. To be more precisely, high-grade osteosarcomas are capable of producing high rates of TGF-β1, -β2 and -β3, whilst in low-grade osteosarcomas the amount of expressed TGF-β1 was reduced. This has in succession an impact on the bone degradation performed by the osteosarcoma cells, which is described in more details in chapter 2.2.5 (Franchi et al., 1998, p. 284).

Parathyroid hormone Type 1 receptor (PTHR1) acts in general as the receptor for parathyroid hormone-related peptide (PTHrP) and parathyroid hormone (PTH). Normally, PTHR1/PTHRP has a significant role in the development of bones. The in vitro study of Yang et al., showed, that the expression of PTHR1 was higher in osteosarcomas, which then resulted in an increased mobility and cell proliferation. Furthermore, the over-expression of PTHR1 has an impact on the osteoblast differentiation, which is decelerated (Yang et al., 2007, pp. 943, 949-953).

2.1.1.4 Osteosarcoma angiogenesis

The tumour angiogenesis[2] is another essential part of the spread and the growth of cancer in general. This process is essential for the continuation of the cancer since the osteosarcoma cells need a supply with nutrients and oxygen, without that, the proliferation would be impossible. Further, these formations also enable osteosarcomas to metastasize, most frequently to the lungs or other bones. Misbalances in the regulation of pro- and antiangiogenic factors occur inter alia under 'tissue hypoxia, acidosis, oncogene activation, and loss of tumour suppressor gene function' (Broadhead et al., 2011, p. 5), which leads to a shift towards the formation of new blood vessels. In osteosarcomas, the expression of the pro-angiogenic vascular endothelial growth factor gene (VEGF) is increased, leading to a stimulation of the formation processes of new vessels, with VEGF-A having the highest angiogenic effect. Further, VEGF also boosts matrix metalloproteinase, which is responsible for the degradation of the extracellular matrix, which is of

---

[2] formation of new blood vessels from existing ones

importance during the curse of this research. In addition to that, the expression of anti-angiogenic factors are attenuated in osteosarcomas, leading to the misbalanced state of angiogenesis (Broadhead et al., 2011, p. 5).

2.1.1.5 Role of osteoclasts in osteosarcoma

In a healthy state of the human body, the skeleton is in a steady state of rebuilding: on the one hand bone degradation, which is done by osteoclasts, and on the other hand the formation of new bone, which is achieved by osteoblasts. Under normal conditions, these two mechanisms are balanced. This equilibrium can be shifted towards bone resorption by the influence of malignant neoplasm diseases like an osteosarcoma (Akiyama, Dass, & Choong, 2008, p. 3461).

To be more precise, both, bone growth and degradation, are mediated and controlled by the receptor activator of nuclear factor κB, short RANK, the corresponding ligand RANKL and osteoprotegerin (OPG). The receptor activator of nuclear factor κB ligand expression is mediated by osteoblastic and bone marrow stroma cells, whilst RANK is expressed on osteoclasts as well as osteoclast predecessors (Trinidad & Gonzalez-Suarez, 2016, p. 1). On the one hand, the binding of RANK and it's ligand on the osteoclast surface leads to the progression of mature osteoclasts and the activation of those (Akiyama et al., 2008, p. 3462). Through the RANK-RANKL binding bone degradation is activated. In turn, the degraded bone matrix releases growth factors. On the other hand, OPG, which is a soluble decoy receptor for RANKL, is capable of throttling the osteoclast differentiation and as a consequence suppresses the activation of osteoclasts (Trinidad & Gonzalez-Suarez, 2016, p. 1). Once the osteoclasts are activated, they start producing proteolytic enzymes, which contain cathepsin K amongst others, which has an important role considering the mineral degradation of the bone matrix and the breakdown of collagen I, osteopontin and osteonectin (Broadhead et al., 2011, p. 7),(Akiyama et al., 2008, p. 3463).
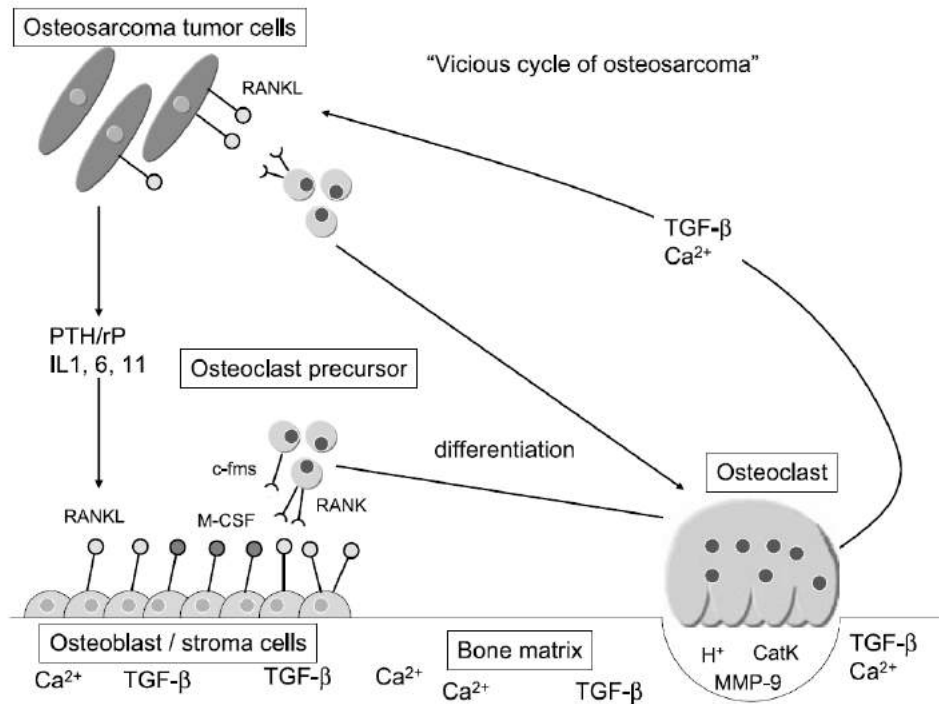
figure 2.2 vicious cycle of osteosarcoma; adapted from (Akiyama et al., 2008)

If one is affected by an osteosarcoma, the mentioned growth factors, which are released by the degrading bone matrix, such as e.g. TGF-β, stimulate the cancer cells and trigger them to produce and release a variety of cytokines, exactly interleukin 6 and 11, and PTHrP. In the next step, these cytokines innervate the osteoclasts and through that stimulate the bone degradation, thus the cancer cells act as mediator in bone degradation. Interleukin-11 and PTHrP further influence directly osteoblasts by inducing the formation of receptor activator of nuclear factor κB ligand (Broadhead et al., 2011, p. 6). Further a variety of studies showed, that osteosarcoma cells have the ability of directly expressing RANKL on their own (Branstetter et al., 2015, p. 60), additionally Akiyama et. al, stated that osteosarcoma expressed PTHrP decreases the production of osteoprotegerin (Akiyama et al., 2008, p. 3465).

To sum up, the RANK-RANKL induced degradation of bone, which leads to the production of growth factors, which then are influencing the osteosarcoma cells and stimulating the growth of them, is ending up in the destruction of the bone and the spread of the tumour – the vicious cycle of osteosarcoma (see figure 3.1) (Trinidad & Gonzalez-Suarez, 2016, p. 1).

2.1.2 Morphology

Although osteosarcoma cells still possess identical properties like osteoblasts, they differ in many major functions, like the production of osteoid, which is up to now only explored to a small amount (Pautke et al., 2004, p. 3746). In a normal, healthy bone tissue, the osteoblasts are producing the extracellular matrix, or more precisely osteoid, which is then mineralized. In contrast to that, it is assumed that the extracellular matrix produced by osteosarcomas is not or not completely mineralized (Nikitovic et al., 2016, p. 1789). Different studies achieved results, that corroborate this theory.

Pautke et al. stated, that in osteosarcomas the expressions of extracellular matrix proteins, which are contributing to the mineralization functions, are different than in normal bone tissue. They found in their tested cell lines, that only very small amounts showed the expression of osteoprotegerin[3], amongst others (Pautke et al., 2004, pp. 3743-3746).

Even further, they found the expression of the matrix metalloproteinase 9 (MMP-9) in osteosarcoma cell lines, which is firstly involved in the degradation of the extracellular matrix (Yabluchanskiy, Ma, Iyer, Hall, & Lindsey, 2013, p. 391), and secondly not found in osteoblasts (Pautke et al., 2004, p. 3746).

Additionally, Benayahu et al. observed the changes in the extracellular matrix protein structure and they found in their research inter alia, that the observed osteosarcoma cell lines lack the biglycan message in the RNA (Benayahu, Shur, Marom, Meller, & Issakov, 2001, pp. 112-113). Biglycan belongs to the proteoglycans and has an important role for the bone mineralization (Parisuthiman, Mochida, Duarte, & Yamauchi, 2005, p. 1878) and the organization of the extracellular matrix (Benayahu et al., 2001, p. 113) in normal bone.

3. Principles of X-Ray diffraction and scattering

3.1 Basic principles

In the first part of this master thesis, all accomplished experiments were carried out using the method of small-angle X-ray scattering (SAXS), which is a non-

---

[3] remind: OPG is capable of throttling the osteoclast differentiation and as a consequence suppresses the activation of osteoclasts (Trinidad & Gonzalez-Suarez, 2016, p. 1)

destructive method. X-rays can be seen as electromagnetic waves with a wavelength in the range of 10^{-10} metres, in the used SAXS-setup the radiation is generated by a Cu anode microfocus x-ray tube and emits the characteristic K-alpha radiation with a wavelength of 0.154 nm/8.05 keV. Two phrases are used when talking in general in this field: (X-ray) diffraction and - scattering. Scattering can be described as the deviation of radiation or moving particles from a straight path caused by one or more local non-uniformities in the medium through which they pass, while diffraction can be seen as apparent bending of waves around small obstacles and the spreading out of waves past small openings.

These two definitions are used in the field of X-Ray diffraction/scattering more randomly, without much difference. The only distinction is that X-Ray scattering is used in the context of scattering on non-periodic structures, whilst X-ray diffraction is used when waves are scattered on periodic structures. It has to be mentioned, that SAXS works for both, non-periodic and periodic structures. Observing the radiation as photons, the energy $\hbar\omega$ can be allocated to a X-ray photon, $\hbar$ is the reduced Plank constant. Further, the state can also be described by $\hbar\vec{k}$, which represents the photon's momentum, $\vec{k}$ is the incident wave vector. During an elastic scattering process, the photon's momentum can be transferred. Through that a new vector $\vec{q}$ can be defined, the so-called scattering vector or wave vector transfer, the unit of this vector is m^{-1} and it is usually given in Å^{-1} (see formula 3.1 and figure 3.1) (Jens Als-Nielsen, 2011).

$$\hbar\vec{q} = \hbar\vec{k} - \hbar\vec{k'} \qquad (3.1)$$

Further, in X-ray diffraction constructive interferences of waves can be described mathematically by the so-called 'Bragg law'. This law states, that integer multiples of the wavelength are equal to the product of the doubled distance d between the lattice planes and the sine of the angle of incidence Θ (see formula 3.2 and figure 3.1) (Jens Als-Nielsen, 2011).

$$n\lambda = 2dsin(\theta) \qquad (3.2)$$
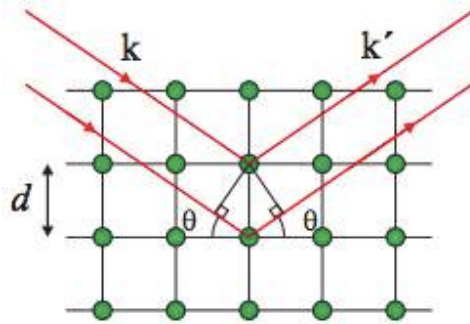
figure 3.1 Basic principle of the Bragg law: k1 the incident beam and k2 the scattered beam; adapted from Jens Als-Nielsen, D. M. (2011). Elements of modern X-ray physics.

3.2 Small angle X-ray scattering

Through equation 3.2, one can recognize that for smaller λ smaller structures can be observed, and for a higher d the angle has to be smaller for a constant wavelength. Small angle X-ray scattering is characterized by $2\Theta \leq 10°$ and therefore structures at the nanometer level can be investigated. In this thesis, this was used to characterize the size and orientation especially of the bone mineral platelets, which then deliver conclusions to the same characteristics of the collagen fibrils.

SAXS analyses are realized by recording the two-dimensional scattering pattern, i.e. the intensity, on an area detector. The pixels of the position-sensitive detector measure the number of scattered photons during the recording time. As a result, an image of the scattered intensity as a function of the wavevector is received (see figure 6.2b). The scattered intensity for a two phase system can be described in general by formula 3.3 (Jens Als-Nielsen, 2011, p. 136).

$$I^{SAXS} = \Delta\rho^2 V_P^2 |\mathcal{F}(q)|^2 \tag{3.3}$$

with

- I, the scattered intensity
- $\Delta\rho$, the difference of the electron density between two phases
- V_p, the volume of the particle
- $\mathcal{F}(q)$, the form factor, depending on size and shape of the particle
- q, the scattering vector

Thus, in the samples which are embedded, the mineral platelets have to show a different electron density to the collagen (so-called contrast) to become visible. The

higher this contrast between the materials is, the better the SAXS results (Schnablegger, 2013, p. 27). In the experiments accomplished in this thesis, hydroxyapatite provides the highest electron density contrast and is therefore mainly responsible for the scattering intensity.

3.2.1 Porod analysis

At large q compared to the size R of the particles, which is equal to qR≫1 (Jens Als-Nielsen, 2011, p. 139), the scattering intensity can be written as (Pabisch, Wagermaier, Zander, Li, & Fratzl, 2013, p. 400)

$$I(q) \xrightarrow[q \to \infty]{} \frac{P}{q^4} + B \qquad (3.4)$$

with

- P, the Porod constant
- B, the constant Background
- q, the scattering vector

4. Quantitative backscattered electron imaging

4.1 Basic principles

The scanning electron microscope (SEM) principally works by the use of a focused electron beam, which hits the sample surface, which is investigated. This process leads e.g. to the emission of secondary electrons, auger electrons, backscattered electrons or X-rays (see figure 4.1). The intensity of the signal strongly depends on the energy of the primary electron beam and on the atomic number Z of the sample. The latter mainly controls which of the scattering events occurs. Further, two types of scattering processes are occurring during the measurement, which are elastic and inelastic scattering (Krinsley, 1998, p. 4).
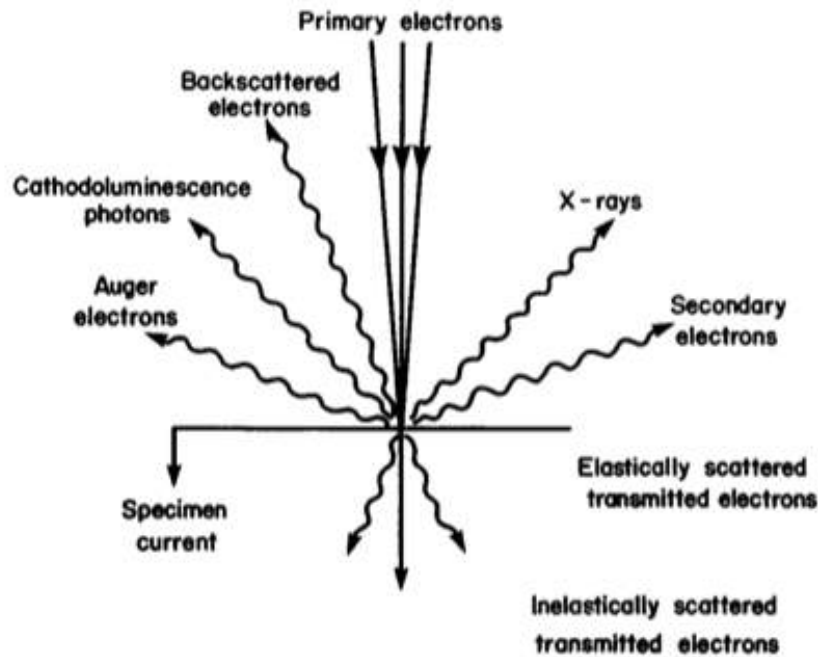
figure 4.1 signals in scanning electron microscopy; adapted from (Krinsley, 1998)

4.1.1 Elastic scattering

Elastic scattering occurs when the primary electrons are in interaction with the specimen, or more exactly with the nuclei, without losing energy or with only a minor reduction of their energy. Yet, their trajectory is influenced. The main part of the elastically scattered electrons are absorbed or pass through the sample, the other part is reflected from the specimen and can be detected as backscattered electrons. These contain information about the atomic weight of the sample's material which allows the distinction between different materials. Therefor the visual assessment of the measurements provide a high atomic contrast, which is used in this thesis to detect differences in the bone mineral density of healthy and tumorous tissue (Krinsley, 1998, pp. 4, 12).

4.1.2 Inelastic scattering

Inelastic scattering of the primary electron beam can occur when again the primary electrons interact with the sample's nuclei with the result of losing some of their energy, or when they collide with electrons of the sample. The first effect results in the emission of X-rays, the latter results in the emission of the loosely bound electrons as secondary electrons (Krinsley, 1998, p. 5).

4.1.3 Influence of the atomic number Z

As already mentioned, the atomic number Z has a high influence on the occurring scattering event. In the presence of samples with low atomic number Z only a small number of the electrons are backscattered, whilst the major part is absorbed. With an increasing atomic number, also the scattering near the surface of the sample rises and through that also the number of backscattered electrons does. For the same energy of the beam, the primary electrons penetrate less deep in materials with a higher atomic number than in comparison to lower Z's, which can be seen in figure 4.2 (Krinsley, 1998, pp. 5-6).
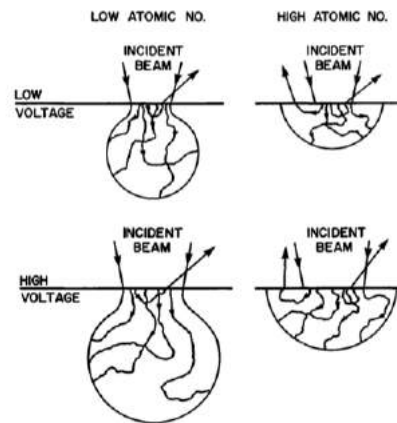
figure 4.2 influence of the atomic number Z on the electron scattering; adapted from (Krinsley, 1998)

The number of backscattered electrons can be given by the backscattered coefficient η (see equation 4.1). Further, it could be proven, that η shows approximately a linear dependency on the atomic number Z until around Z=30. Above that value, the resulting curve degenerates, which can be seen in figure 4.3 (Krinsley, 1998, p. 6).

$$\eta = \frac{number\ of\ backscatterd\ electrons}{number\ of\ incident\ electrons} \qquad (4.1)$$
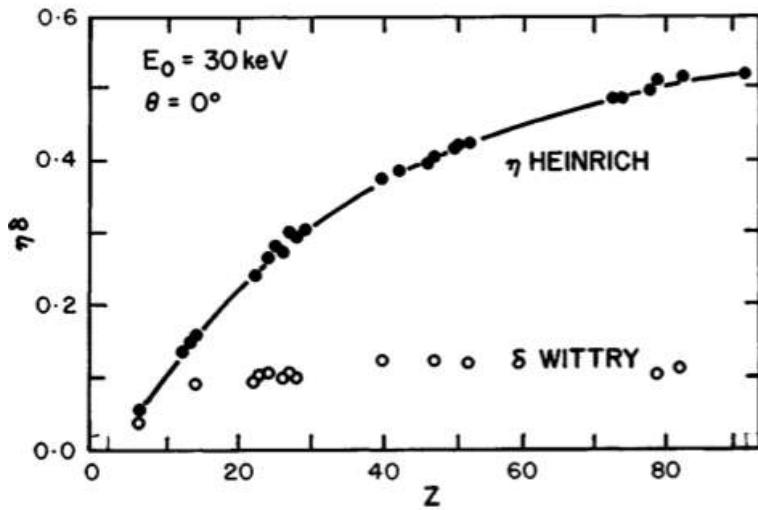
Z	η	Z	η	Z	η	Z	η
1	0.010	24	0.282	47	0.412	70	0.482
2	0.021	25	0.291	48	0.415	71	0.485
3	0.031	26	0.300	49	0.419	72	0.487
4	0.043	27	0.309	50	0.423	73	0.490
5	0.054	28	0.317	51	0.426	74	0.492
6	0.066	29	0.325	52	0.430	75	0.495
7	0.079	30	0.332	53	0.433	76	0.498
8	0.093	31	0.339	54	0.436	77	0.501
9	0.107	32	0.345	55	0.439	78	0.504
10	0.121	33	0.350	56	0.443	79	0.507
11	0.136	34	0.355	57	0.446	80	0.509
12	0.150	35	0.360	58	0.449	81	0.510
13	0.164	36	0.365	59	0.452	82	0.512
14	0.176	37	0.370	60	0.455	83	0.513
15	0.189	38	0.375	61	0.458	84	0.515
16	0.201	39	0.379	62	0.461	85	0.516
17	0.212	40	0.384	63	0.463	86	0.517
18	0.223	41	0.388	64	0.466	87	0.518
19	0.233	42	0.392	65	0.469	88	0.519
20	0.243	43	0.396	66	0.472	89	0.520
21	0.253	44	0.400	67	0.474	90	0.521
22	0.263	45	0.404	68	0.477	91	0.522
23	0.273	46	0.408	69	0.479	92	0.523

$E_0 = 30\,\text{keV}$

$\theta = 0°$

η HEINRICH

δ WITTRY

figure 4.3 left: Relationship between backscattering coefficient and the atomic number Z (data from Heinrich(1966)); right: backscattered coefficients according to the corresponding atomic number (Data from Bishop)); both figures adapted from (Krinsley, 1998, pp. 5-6)

II. Methods

5. Sample preparation

The samples for this research were kindly provided by the Medical University of Graz by Prof. Dr. Andreas Leithner. A 19-year-old male patient, who suffered from an osteosarcoma located at the distal femur, had to surgically remove parts of the femur. These parts were then used for this research. It was divided in four parts (see figure 5.1), one part where the osteosarcoma was assumed to be, one part where only normal bone tissue was assumed, one part where both, tumorous and healthy bone tissue could be present ("crossing") and one part which represented the resection margin. All sample blocks were fixed in formalin, dried in an ascending ethanol series and then embedded before this research project in Technovit® 9100, which is based on polymethylmethacrylate (PMMA) and is used especially for the embedding of mineralized tissue.
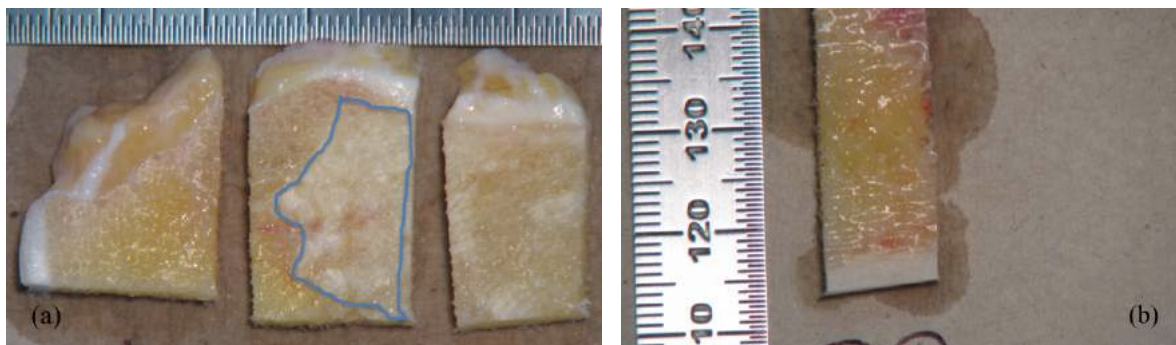
figure 5.1 different types of the bone samples: (a) left to right normal bone tissue, tumorous tissue, crossing between normal and tumorous tissue; (b) resection margin

5.1 SAXS sample preparation

Most of the slices, which are necessary for the SAXS measurement, were prepared prior to this thesis. Additionally, the slices of the tumor tissue block still had to be made, which was done by the same procedure. That was used to produce the samples of the normal bone tissue, the crossing tissue and the resection margin.

For cutting the specimen an Accutom-50 diamond saw from Struers was used. The blocks were chucked in the sample holder and cut with a diamond wheel. Through that it was possible to produce slices with a thickness in the range of 200 to 300 μm, which is an important premise for the following SAXS experiments. The feed rate during the cutting process was 0.01 mm per second with 3000 rotations per

minute. Additionally, the wheel was cooled with a mixture of water and Corrozip, which is protecting the machine from corrosion.

5.2 qBEI sample preparation

For the quantitative backscattered electron imaging measurements, the bone tissue slices had to be fixed on the SEM sample holder. Therefore, the samples were glued on the holder by a two-component glue, a UHU® Plus Endfest, which is based on an epoxy-resin formulation. Further, reference samples had to be fixed to interpret the intensities from BEI. Graphite, aluminum and magnesium fluoride were used as standard specimen. To fasten the hardening process, the sample holder was placed for about two hours at 60° in an oven. Even after that, it has to cure for at least another 12 hours to reach the optimal hardness.

To receive valid results of these measurements, the samples on the holder, including the bone specimen and the two reference materials, had to be ground in one plane, to ensure that no topological factors would influence the measurement. This was achieved by grinding the samples on the Struers grinding instrument Planopol-3. All specimen were ground under wet conditions (to avoid any cracks) with Struers waterproof silicon carbide abrasive papers. The first grinding process was made with grain size 500, with the next sizes being 1000, 2000 and 4000. In the final step the samples were polished by the use of an AP-A suspension from Struers, which is an agglomerated alpha alumina suspension.

6. SAXS measurement

6.1 SAXS setup

All SAXS measurements were done at the University of Natural Resources and Life Sciences Vienna.

The experiments were carried out using a "Rigaku S-Max 3000". The X-ray beam was generated from the "MM002+", a sealed microfocus x-ray tube with a copper target, which works at 45 kV and 0.88 mA. As detector a gas filled, position sensitive Gabriel-type multi wire detector, the "Triton 200", was used. The generated X-rays were collimated through a system of pinholes, so that the final beam had a beam size of approximately 200 μm, when hitting the specimen. The

used pinholes had a diameter of 400, 200 and 700 μm and were installed in the system in that order going from the X-ray source towards the detector (Gruenewald et al., 2016, pp. 449-450).

The setup can be seen in figure 6.1 and a simplified process of a measurement in 6.2, the devices are simplified listed below.

1. The X-ray source
2. Pinhole 1, diameter 400 μm
3. Pinhole 2, diameter 200 μm
4. Pinhole 3, diameter 700 μm
5. The vacuum chamber
6. The 2D-detector

figure 6.1 Setup of the SAXS device at the laboratory of the BOKU

Through this setup an effective q-range from 0.02 to 0.45 Å^{-1} was reached in the course of these experiments. Due to the different scattering properties of the different samples, the current of the X-ray source had to be adjusted for each specimen, between 0.22 and 0.5 mA, which included also measurements of the background. The working distance between the sample and the 2D-detector within this thesis was 520 mm. The sample was fixed on a sample holder in the vacuum chamber, which was then evacuated to a pressure of 10^{-3} mbar. The holder was mounted on a motor, so that the sample was able to move either horizontally or vertically within the chamber. In this way, it was possible to measure major parts of the bone samples, the step size for a movement after finishing a measured point was 200 μm.
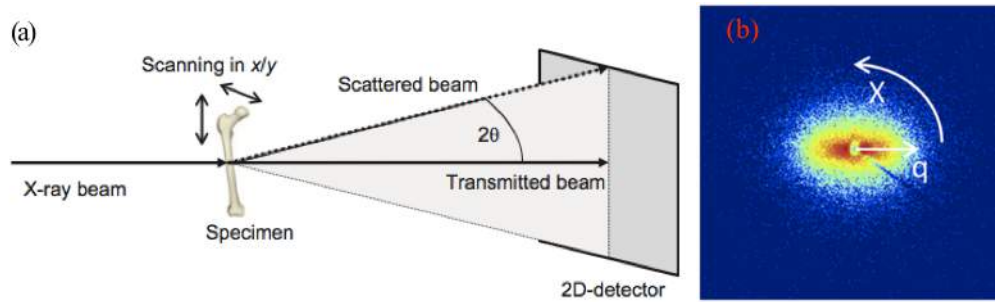
figure 6.2 (a) principle setup of the SAXS system; adapted from (Pabisch et al., 2013) (b) typical SAXS scattering intensity pattern, including the different integration directions; adapted from (Gruenewald et al., 2016)

In all experiments silver behenate, where the lattice parameters are well known, was used for calibration. This is necessary to determine the exact distance of the sample to the detector and even further to define the beam center.

Prior to starting a long term measurement on the whole sample, some points of each specimen had to be controlled in detail. This is due to the fact, that the detector has to be treated carefully by the means of counts per pixel and overall counts of the photons. Thus, if the intensity was too high, the standard current of 0.88 mA of the X-ray source was reduced. Generally, it can be said that the current for all bone samples had to be reduced, the degree of the reduction was mainly determined by the thickness and the type of the bone samples.

6.2 Data integration

To obtain results from the measurements, the 2D data has to be integrated. Depending on the desired information, this can be done in different ways (see figure 6.2b). The first way is to integrate the data radially (formula 6.1, figure 6.3b), which is dependent on length of the scattering vector, the other option would be to integrate azimuthally (formula 6.2, figure 6.3a), which is dependent on the azimuthal angle (Pabisch et al., 2013, p. 397).

$$I(q) = \int_0^{360} I(\chi, q) d\chi \qquad (6.1)$$

$$I(\chi) = \int_{q_{min}}^{q_{max}} I(\chi, q) dq \qquad (6.2)$$
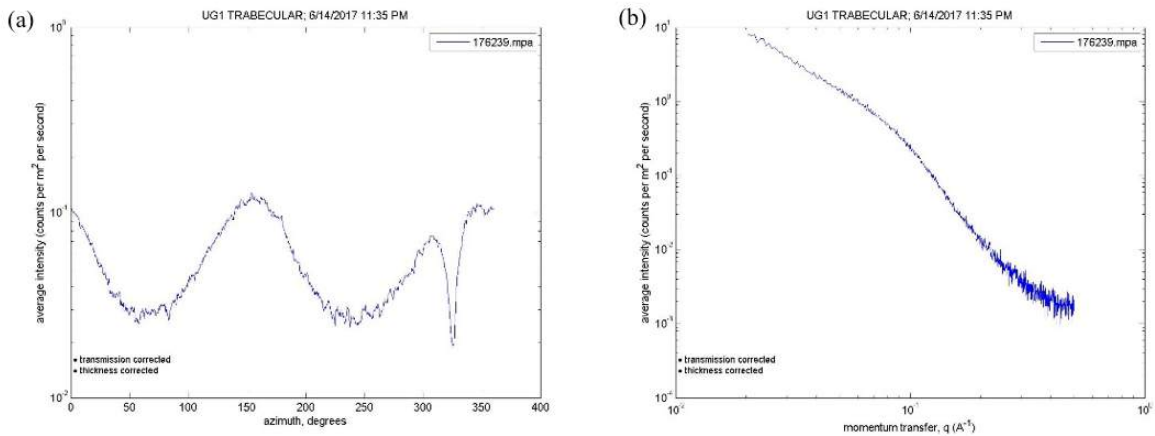
figure 6.3 (a) azimuthal integration of the data; (b) radial integration of the data, intensity in arbitrary units

The beamstop shadow, that can be seen in figure 6.3(a), had to be corrected in order to be able to calculate the degree of orientation in the right way. This was done in mathematica by transposing data points, which were 180° separated from the beamstop arm, to the located shadow and was implemented by Dr. Gruenewald before. Figure 6.4(b) shows a fitted curve, where the correction is already made.

6.2.1 The radial integration

The radial intensity profile I(q) can be used to determine the thickness of the particles, in this thesis this is particularly used to establish the thickness of the mineral particles.

6.2.1.1 The T-parameter

The thickness of the particles can be expressed by the so-called T-parameter. It has to be mentioned, that this parameter calculates only the smallest dimension, and does not consider the shape of the particles (Gourrier et al., 2010, p. 1386). Thus, considering the bone mineral particles, which are assumed to be platelets, the T-parameter describes the thickness of them.

By the use of the Porod analysis, together with the invariant, for high q from chapter 3.2.1 the T-parameter of the mineral platelets can be determined. Therefore, in the first step the Porod constant P and the background B from equation 3.4 have to be determined.

This can be reached by plotting $I(q) \cdot q^4$ versus q^4 for high q, which is the so-called Porod plot. In the calculation of this parameter a two-phase system is assumed and

further, the mineral volume fraction ϕ is set to 50%, which is also limiting the accuracy of this parameter (Gourrier et al., 2010, p. 1387). This was achieved by plotting and fitting the curve in Wolfram Mathematica.

The definition of the T-parameter and the invariant J can be seen in formulas 6.3 and 6.4.

$$T = \frac{4 \cdot J}{\pi \cdot P} = \frac{4}{\pi \cdot P} \int_0^\infty q^2 [I(q) - B] dq \tag{6.3}$$

$$J = \int_0^\infty q^2 [I(q) - B] dq \tag{6.4}$$

with

- P, the Porod constant
- B, the constant background
- q, the scattering vector
- I(q), the radial intensity profile

The calculation of the invariant was done by plotting $q^2[I(q) - B]$ against q, which is referred to as the Kratky plot (Pabisch et al., 2013, p. 401). This was again accomplished in Mathematica by computing the area under the plot. Due to the fact that in the experiments the q-range is limited, the bounds of the integration have to be adapted. Everything below the lower limit q_{min} is assumed to linearly decrease (Pabisch et al., 2013, p. 402), whilst the upper limit q_{max} can be approximated with the use of the Porod's law, with the result that $J = \int_{q_{max}}^\infty q^2 I(q) dq = P/q_{max}$. Through the determination of the integral and the Porod constant it was then through equation 6.3 possible to receive values for the T-parameter (Gourrier et al., 2010, p. 1387).

6.2.2 Stack of cards model

Additionally, another model, the so-called stack of cards model, for the calculation of the T-parameter was applied in the progress of this thesis.

In this model, the shape of the particles is included by assuming that the mineral particles are platelets with a local parallel arrangement. These assumptions are

pooled in a rescaled function to which the model is fitted (see formula 6.5) (Gourrier et al., 2010, pp. 1386-1388).

$$G(x) = x^2 I(\tfrac{x}{T})/(JT^3)$$

(6.5)

with the dimensionless parameter:

$$x = qT$$

(6.6)

In comparison to the applied model before, the T-parameter in this model is now a fit parameter. The stacked arrangement of the mineral platelets is described through formula 6.7, which is used for fitting the data (Gruenewald et al., 2016, pp. 450-451).

$$G(x) = \frac{4}{\pi} \frac{x^2(\alpha-1)(\alpha^2+\beta^2)}{(x^2+\alpha^2+\beta^2)^2+4\alpha^2\beta^2}$$

(6.7)

The fit parameter α and β describe the damping of the oscillations and the degree of spatial correlation between sequential mineral particles, respectively (Gruenewald et al., 2016, p. 451).

The data can then be fitted by equation 6.8 and since the T-parameter is in this model a fit parameter it can directly be determined through the fit (see equation 6.10) (Gourrier et al., 2010, p. 1388).

$$q^2[I(q) - B] = \frac{\pi}{4} PT^2 G(x)$$

(6.8)

6.2.3 The azimuthal integration

The second approach to get information about the measured samples is to integrate the data azimuthally. In this way, the azimuthal intensity profile I(χ) can be used to gain information about the orientation of the particles. A first estimation can be directly made within a scattering image.

When receiving an elliptical scattering pattern, the azimuthal intensity profile shows two Gaussian peaks that are separated by 180° (see figure 6.4). The corresponding χ values to these peaks represent the preferred orientation of the investigated particles, which are here the mineral platelets. One has to pay attention, that these orientations are rotated by 90° (Roschger et al., 2001, p. 129).

Otherwise, a circular scattering pattern suggest no preferred orientation of the platelets and indicate an isotropic point (see figure 6.5).
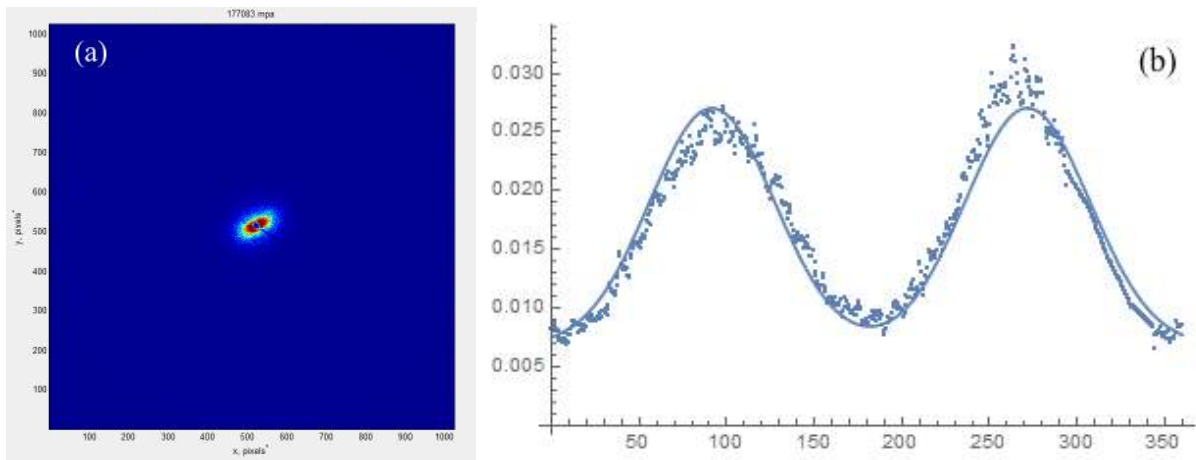
figure 6.4 (a) typical obtained scattering pattern and (b) related azimuthal integration; intensity in arbitrary units (y-axis), x-axis belongs to azimuthal angle;
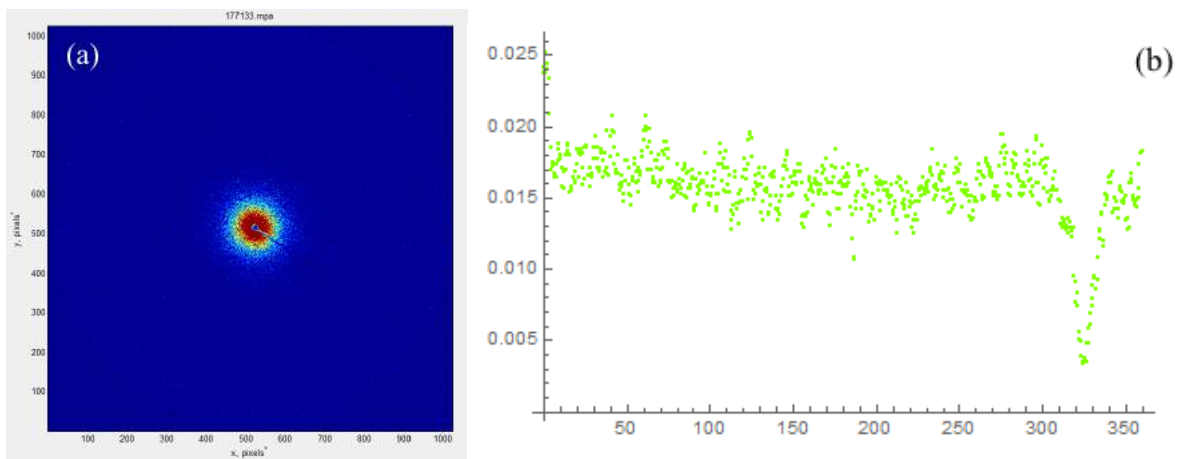
figure 6.5 (a) typical obtained scattering pattern and (b) related azimuthal integration of an isotropic point; intensity in arbitrary units (y-axis), x-axis belongs to azimuthal angle;

6.2.3.1 The ρ-parameter

The so-called ρ-parameter is used to determine the degree of alignment of the mineral platelets in the specimen, and can be determined by the use of the azimuthal intensity profile. In detail, this is first done by fitting the curve (see formula 6.9 and figure 6.4b). By calculating the ratio of the area under the two peaks and the area under the two peaks together with the background (see formula 6.10 and figure 6.6), the ρ-parameter can be determined (Pabisch et al., 2013, p. 399). The fitting of the azimuthal intensity profile was again accomplished in Wolfram Mathematica.

$$I(\chi) = B + a \cdot (e^{-\frac{(\chi-b)^2}{2c^2}} + e^{-\frac{(\chi-b-180)^2}{2c^2}}) \qquad (6.9)$$

$$\rho = \frac{A_1 + A_2}{A_1 + A_2 + B} \qquad (6.10)$$

with

- χ, the azimuthal angle
- a, the height of the peak of the gaussian curve[4]
- b, the position of the observed peak[2]
- c, the width of the gaussian curve at middle height
- A_1, the area under the first peak
- A_2, the area under the second peak
- B, the constant background
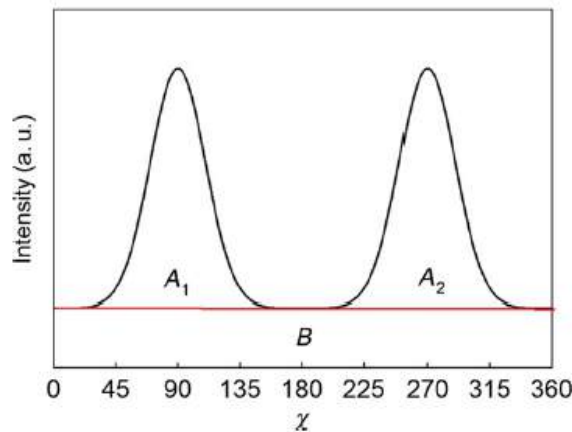
figure 6.6 Definition of the areas, that are used for the calculation of the ρ-parameter; adapted from (Pabisch et al., 2013)

The combined area under the two peaks can be seen as the number of mineral platelets with a preferred orientation, whilst the amount of the constant background represents those without any favored alignment.

---

[4] https://en.wikipedia.org/wiki/Gaussian_function

7. quantitative backscattered electron imaging

7.1 scanning electron microscope setup

The standard scanning electron microscope (SEM) consists of the electron beam column, a sample stage, a detector, which are held under vacuum, and a signal processing system, as main parts (see figure 7.1). The SEM beam column is made up by the electron gun, the magnetic lenses and the apertures. (Wang & Petrova, 2012, pp. 107-108). In this thesis, the experiments were performed on a quanta 250 FEG from the company FEI. The electron beam, which is used to investigate the specimen, is produced by a Schottky diode, which is a field-emission gun.

The produced electron beam is then downsized and focused by electromagnetic lenses. This is also the step where the spot size on the specimen is determined (Wang & Petrova, 2012, p. 109). In the process of these experiments a spot size of 3.0, which is in arbitrary, machine specific units, was used.
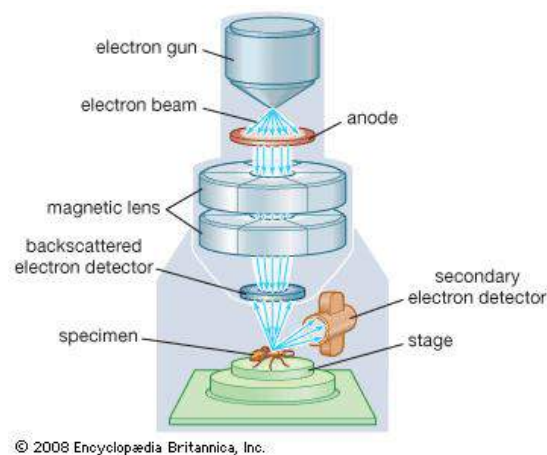
figure 7.1 principle setup of a scanning electron microscope; adapted from https:// www. Britannica.com /technology/scanning-electron- microscope

In a first attempt, the prepared samples were coated with a thin carbon layer through a sputtering process and then mounted in the chamber. It turned out, however, that the carbon sputtering equipment did not work properly. The needed vacuum couldn't be reached anymore and thus, this affected the coating of the samples. Further, after the first measurements with the carbon sputtered samples the grey value scale was extremely limited, it was only possible to reach grey values in a range of about 30 steps. Therefore, it was decided to sputter the

specimen with gold. This change enabled the determinations of grey values in a much higher dynamic range. It was also checked, if the gold layer had any influences on the overall evaluation of the bone mineral density. Therefore, a specimen was tested without, one layer and finally two layers of gold. The results showed almost the same values for the mineral volume fraction, and thus, sputtering with gold should have no influence on the mineral analysis.

Further, the measuring setup had to be adjusted to guarantee applicable images. For this purpose, the working distance was adjusted to 10 mm, whilst the energy of the electron beam was set to 20 kV.

7.2 Determination of the bone mineral density through qBEI

To get access to the mineral density of the investigated samples, one has to do a calibration of the grey values with the help of reference samples. The measurements were based on the method of Roschger et.al. In the experiments during this thesis, magnesium fluoride and Carbon were used as reference materials. In the first testing experiments aluminum was used as second reference material. The grey values differed completely from the estimated values. One explanation could be, that it was either not pure aluminum and instead aluminum oxide, or that through the longer exposure time in air, an aluminum oxide layer could have been formed on the surface of the sample and influenced through that the grey values. Therefore, the reference sample was changed to magnesium fluoride

The application of the method of Roschger et.al. can be achieved by using the different contrast through different atomic numbers Z of the materials, as described before in the theory section.

The grey levels of the reference samples (where the atomic number is known, with $C: Z = 6$; $MgF_2: Z_{mean} = 10.17$) were determined. Further, the brightness and the contrast were kept fixed. Through the knowledge of both, grey values and atomic numbers of the two reference specimen, one can determine a linear calibration line between atomic numbers and grey values (see figure 7.2). As a consequence, it is possible to calculate the grey value of a material, if the effective atomic number is known (Roschger, Fratzl, Eschberger, & Klaushofer, 1998, p. 321).
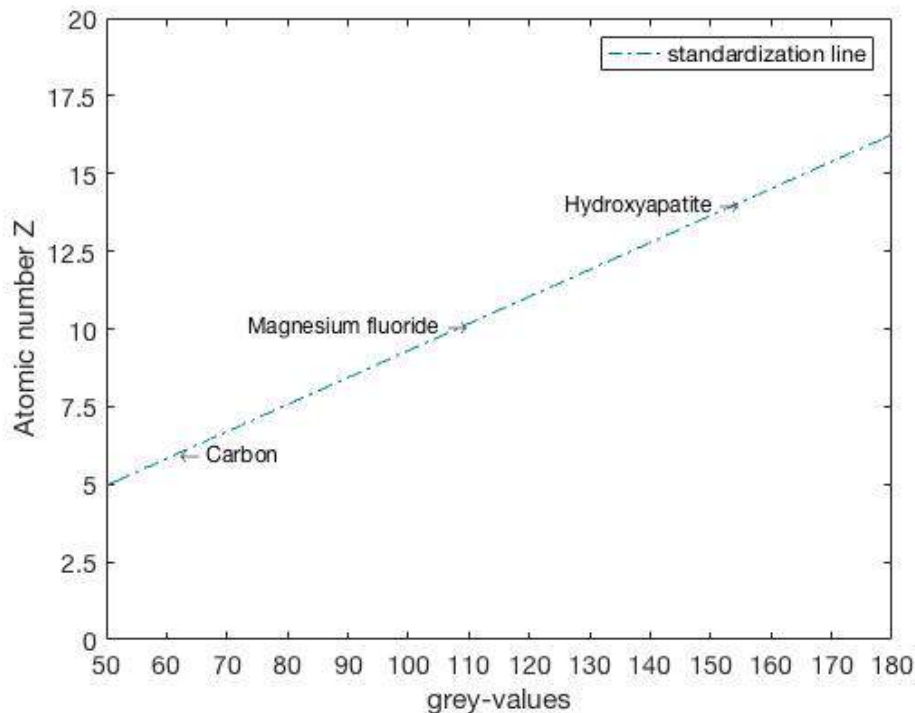
figure 7.2 received calibration line in matlab between the obtained grey values and the atomic number Z, here for the tumorous tissue sample TU3

The process of computing the calibration line has to be done separately for every sample.

Since in bone calcium has the highest atomic number and influences the intensity of the backscattered electrons the most, one can obtain calcium concentrations from the delivered images (Roschger et al., 1998, p. 319).

For this purpose, it is necessary to transfer the grey values into wt% calcium. This can be done by using the same scheme as before. To receive a standardization line between wt% calcium and the grey values, one has to know at least two reference samples, where the composition of the material and the wt% calcium is known. Osteoid represents the un-mineralized bone matrix with 0 wt% calcium, and pure hydroxyapatite, with 39.86 wt% calcium. Through the calculation of the mean atomic number Z (HA: Z=14.06), the grey value can be extrapolated for hydroxyapatite. (Roschger et al., 1998, p. 321).

Roschger et. al. found that osteoid had almost the same grey value as graphite, which we therefore used as reference for wt% calcium. In this way, it was possible to transfer the grey value of the measured bone areas into values of wt% calcium. One of the determined calibration lines can be seen in figure 7.2.
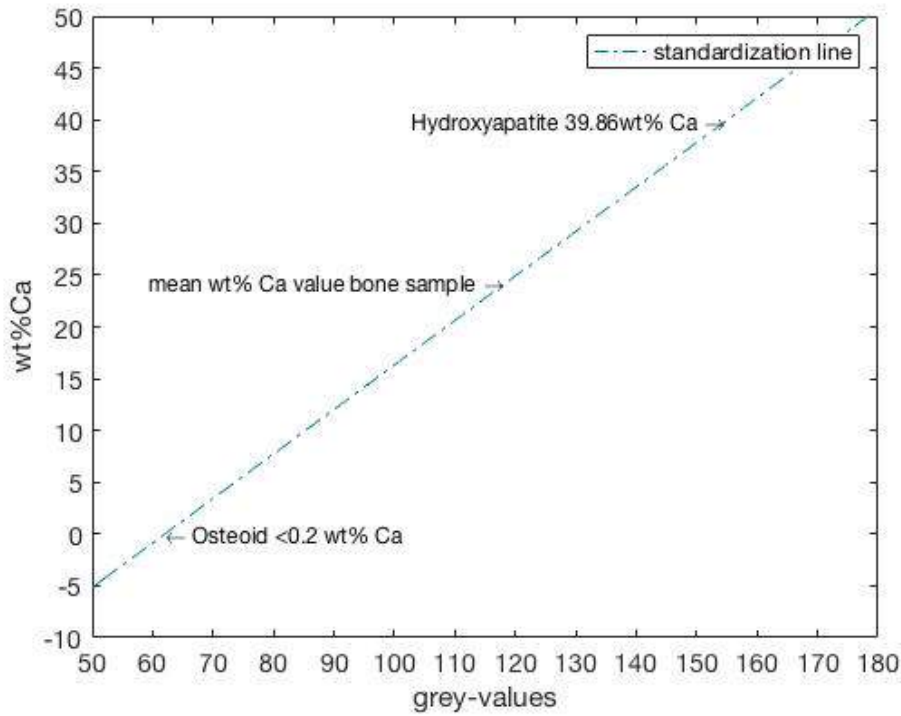
figure 7.3 received standardization line in matlab for transforming the obtained grey values into wt% calcium, here for the tumorous tissue sample TU3

Thus, finally it is possible to calculate in MatLab with self-written routines the weighted mean calcium concentration C_{mean} of the investigated bone area. These values can then be used to calculate the total mineral fraction in the bone area. This was done by using formula 7.1 and 7.2 from Zizak et.al (Zizak et al., 2003, p. 212)

$$\phi = HA_{vol} = \frac{HA_{weight}}{HA_{weight} + (1 - HA_{weight}) \cdot (\frac{\rho_{HA}}{\rho_{org}})} \qquad (7.1)$$

$$HA_{weight} = 2.51 \cdot Ca_{mean} \qquad (7.2)$$

with

- ϕ, the mineral volume fraction
- HA_{vol}, the hydroxyapatite volume fraction
- HA_{weight}, the weight fraction of hydroxyapatite
- ρ_{HA}, the density of hydroxyapatite (literature: 3.18 g/cm³)
- ρ_{org}, the density of the organic matrix (literature: 1.41 g/cm³)

Due to the fact that osteosarcoma cells produce immature bone matrix, which is assumed to show a significant difference in structure and degree of mineralization, this assumption can be used in the backscattered electron imaging experiments to detect these areas. As already mentioned, calcium, as part of hydroxyapatite, has the most influence on the backscattered electron intensity. It can be assumed that also the calcium concentration in tumorous bone should differ to normal bone regions. Thus, the method of qBEI can be used to distinguish between bone parts that are infested by cancer and healthy parts.

III. Results

8. Results of the SAXS measurements on the bone samples

In this chapter, all SAXS results of the different kinds of bone tissue samples are displayed. This includes the evaluations of the thickness of mineral platelets by two different models as well as the characterization of the degree of orientation of the particles. The white and black areas in the visual evaluations of the bone sample thickness are referred to areas where no bone tissue and only air or resin was present, respectively. The x- and y-axes in the graphics describe the local position on the sample holder in millimeters, the scale for the T-parameter is in units of Ångström (Å), the scale of the ρ-parameter is dimensionless and ranges from 0 to 1, representing zero and full orientation, respectively. In figure 8.1 the areas of the available bone samples, which were measured in the course of this thesis, are shown.
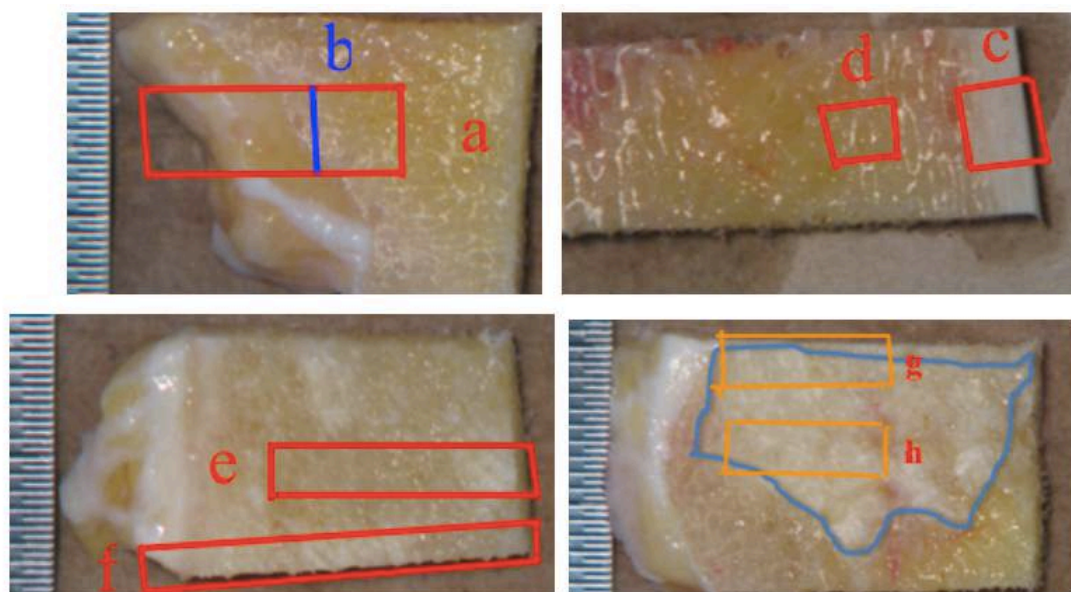
figure 8.1 measured areas of the bone samples (a) normal tissue NO1, (b) normal tissue NO2, (c) resection margin cortical bone RR1, (d) resection margin trabecular bone RR2, (e) crossing sample UG1, (f) crossing sample UG1_bottom, (g) tumor tissue TU1, (h) tumor tissue TU3

8.1 Results resection margin samples

8.1.1 T-parameter

For the investigation of the resection margin, two samples were available, it was known before that in this specimen were free of osteosarcoma tumor cells. Thus, these samples served as reference material for all other measurements. Due to the

fact that the areas of cortical and trabecular bone showed different scattering intensities, the measurements of these regions where split up and then evaluated separately.

The T-parameter showed identical values for both, cortical and trabecular bone areas. The thickness of the mineral particles determined by the stack of cards model was on average 33.5 Å (SD: 1.36 Å). In comparison to that, the averaged thickness calculated by the Porod analysis and equation 6.3 delivered a value of 28.5 Å (SD: 1.09 Å) on average. When studying the figures, no region displays a significant difference of thickness. To simplify reading, the Porod method to determine the T-parameter is from now on called the 'standard model'. The results are illustrated in figures 8.2 to 8.5 and split up in cortical and trabecular bone areas.

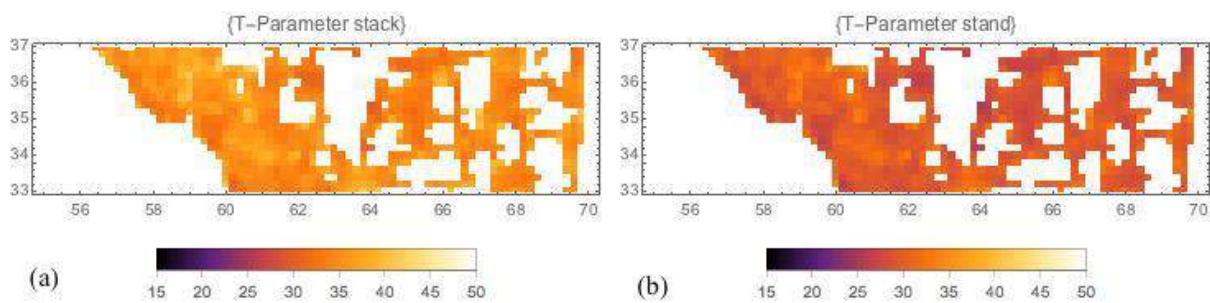*Region of resection margin RR1: cortical bone*
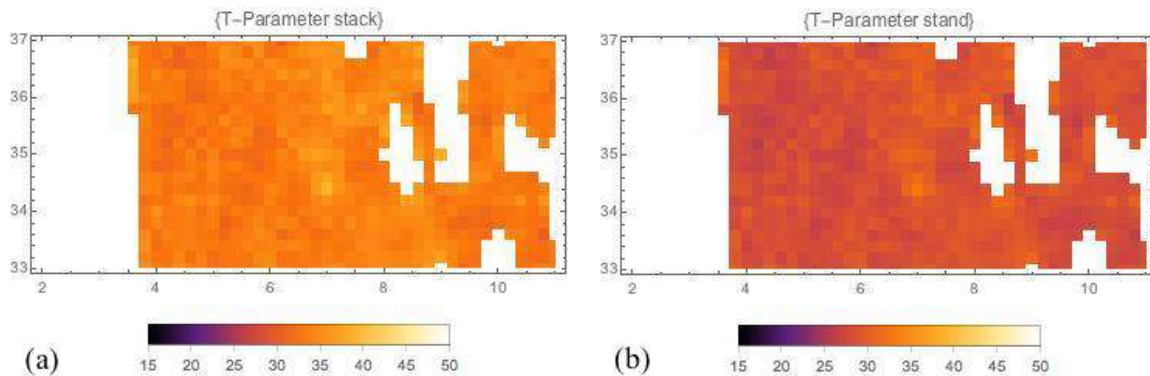
figure 8.2 determined T-parameter plot from the SAXS measurements on the resection margin (cortical) sample 1 for both models: (a) stack of cards model; (b) Porod analysis; the x-axis and y-axis belong to the measured positions in millimetres, T-parameter values in units of Å

Region of resection margin RR2: cortical bone
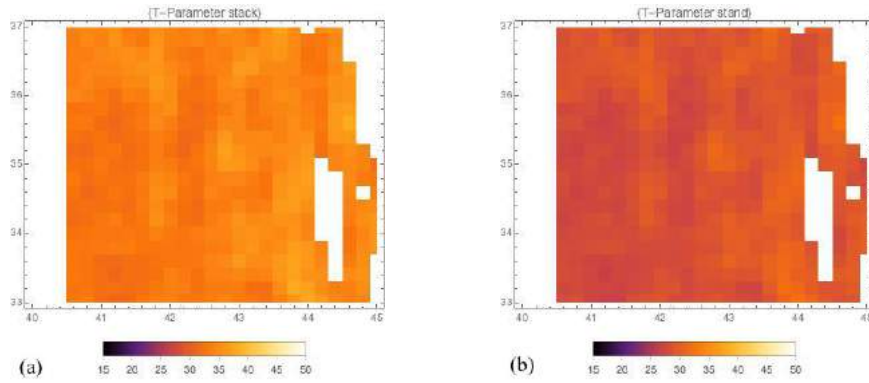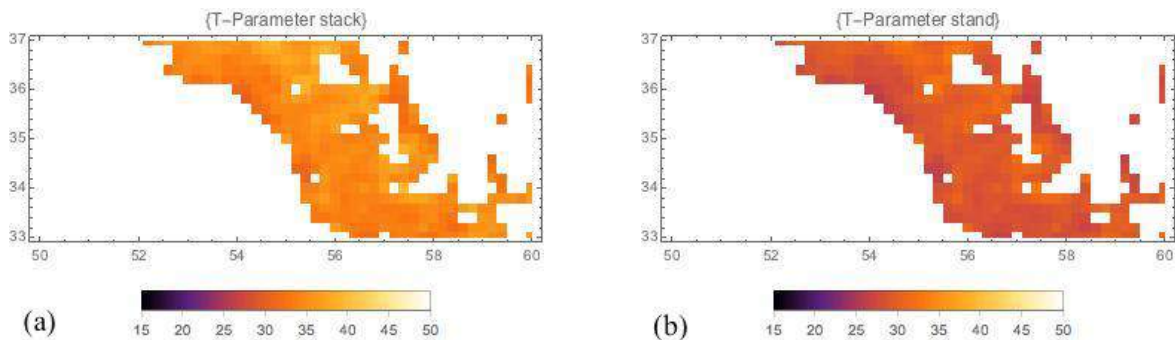

figure 8.3 determined T-parameter plot from the SAXS measurements on the resection margin (cortical) sample 2 for both models: (a) stack of cards model; (b) Porod analysis; the x-axis and y-axis belong to the measured positions in millimetres, T-parameter values in units of Å

Region of resection margin RR1: trabecular bone
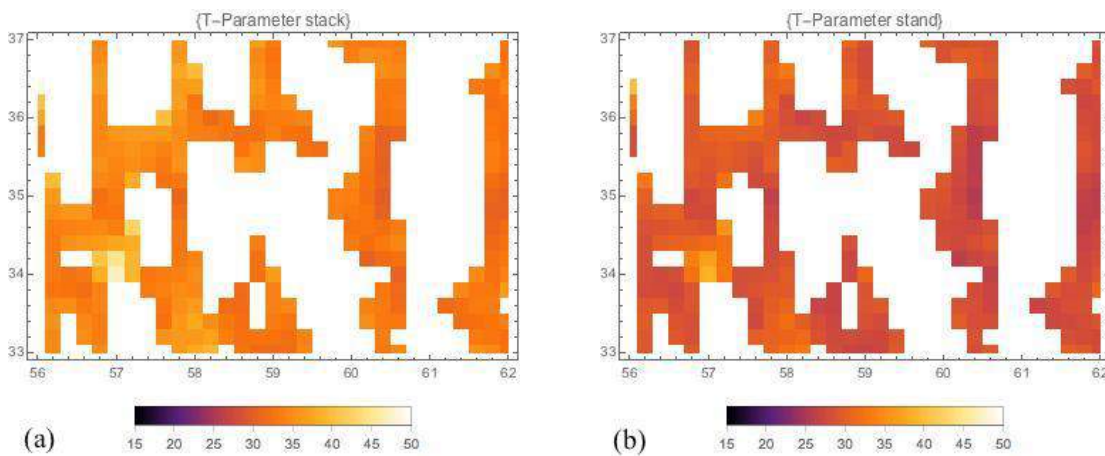
figure 8.4 determined T-parameter plot from the SAXS measurements on the resection margin (trabecular) sample 1 for both models: (a) stack of cards model; (b) Porod analysis; the x-axis and y-axis belong to the measured positions in millimetres, T-parameter values in units of Å
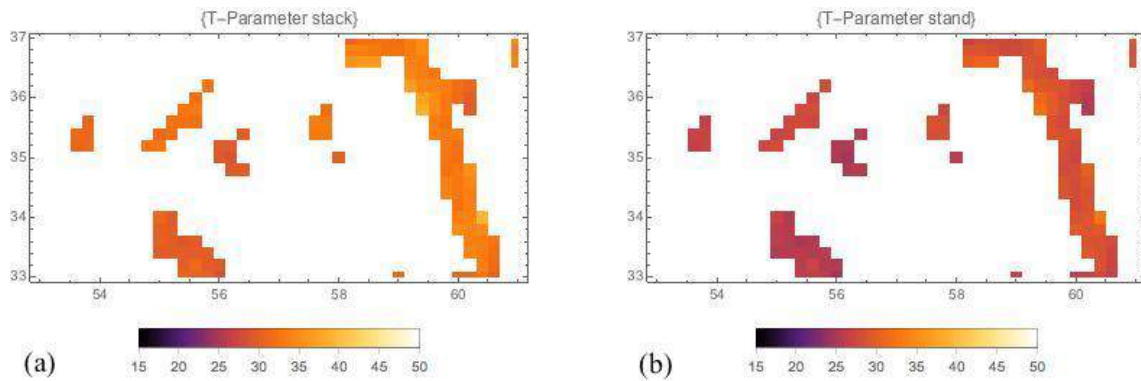
figure 8.5 determined T-parameter plot from the SAXS measurements on the resection margin (trabecular) sample 2 for both models: (a) stack of cards model; (b) Porod analysis; the x-axis and y-axis belong to the measured positions in millimetres, T-parameter values in units of Å

8.1.2 ρ-parameter

Besides the calculation of the T-parameter, also the ρ-parameter, which represents the degree of orientation of the particles, was calculated. For a clear representation purpose, the measured isotropic points, which have, due to the isotropy, an assigned ρ-value of nil, got assigned a new value of 0.05. Due to this adaptation, the isotropic points can now be distinguished from unimportant areas like air or resin. In the graphics, those points that are now representing the ρ-parameter of the isotropic bone areas, are denoted as black dots. The white areas in these plots again represent areas where only air or resin was present. Further, attention has to be paid when studying the histograms of the ρ-parameter in the chapter *discussion*, that all isotropic points are there summarized and represented by the first bar at 0.05.

The delivered plots showed almost a homogeneous distribution around the value of 0.5, with almost no points of isotropy. The exact measured values are displayed then in chapter 8.5, the mean averages for cortical and trabecular areas were 0.54 (SD: 0.13) and 0.50 (SD: 0.17) respectively.

*Region of resection margin RR1 and RR2: cortical bone*
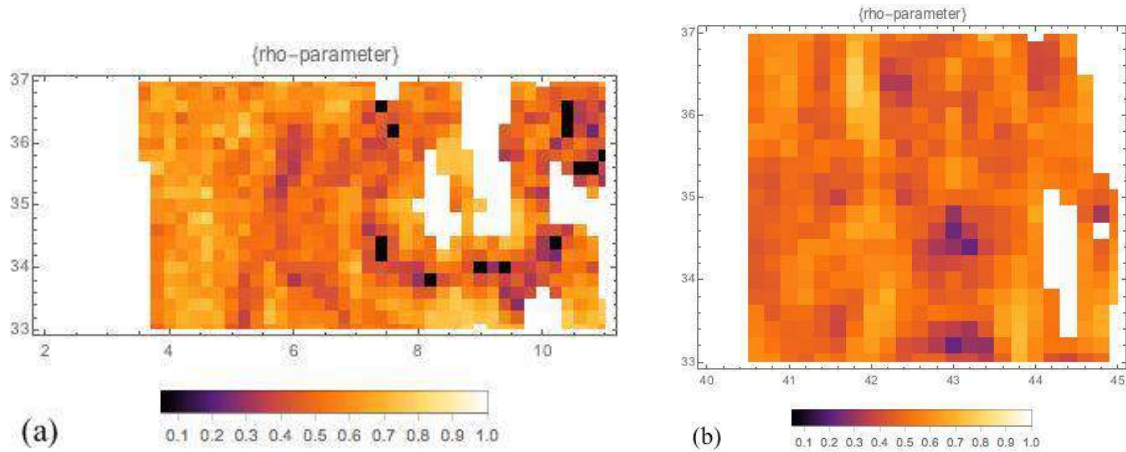
figure 8.6 determined degree of orientation plot from the SAXS measurements on the resection margin (cortical) 1 (left) and 2 (right); the x-axis and y-axis belong to the measured positions in millimetres,

Region of resection margin RR1 and RR2: trabecular bone
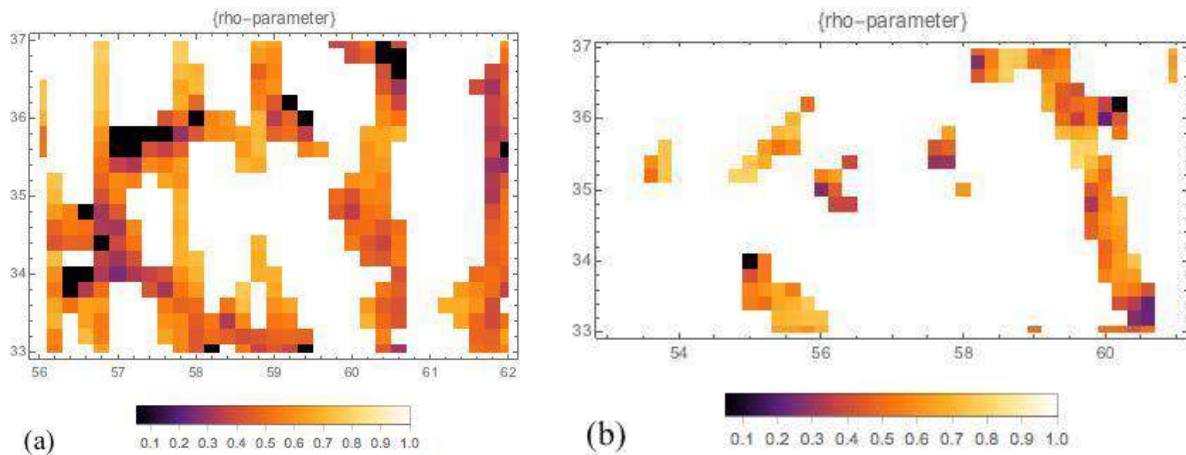
figure 8.7 determined degree of orientation plot from the SAXS measurements on the resection margin (trabecular) samples 1 (left) and 2 (right); the x-axis and y-axis belong to the measured positions in millimetres,

8.2 Results normal bone tissue samples

8.2.1 T-parameter

Next, the measurements were done on the normal tissue samples, where it was assumed that also only healthy bone tissue was present. It was also possible to measure both, the cortical and trabecular bone region of the normal tissue sample 1, in one measurement routine, since here, both areas showed almost the same scattering intensities. The measurement of normal tissue sample 2 only included the cortical bone area.

The measured thicknesses of the normal tissue samples were in both models clearly in the same range as those of the resection margin samples. Further, the averages of the thicknesses are 35.1 Å (SD: 2.08 Å) in the stack of cards model and 29.5 Å (SD: 1.65) in the standard model for NO1 (NO2: 34.69 Å (SD:1.74 Å), 29.28 Å(SD: 1.39 Å)). The thickness is overall almost equal, also the areas of cortical and trabecular bone show the same range of thickness. The evaluated results of the two measured areas can be seen in figures 8.8 and 8.9.

Region of normal bone tissue NO1

figure 8.8 determined T-parameter plot from the SAXS measurements on the normal bone tissue sample 1 for both models: (a) stack of cards model; (b) Porod analysis; the x-axis and y-axis belong to the measured positions in millimetres, T-parameter values in units of Å
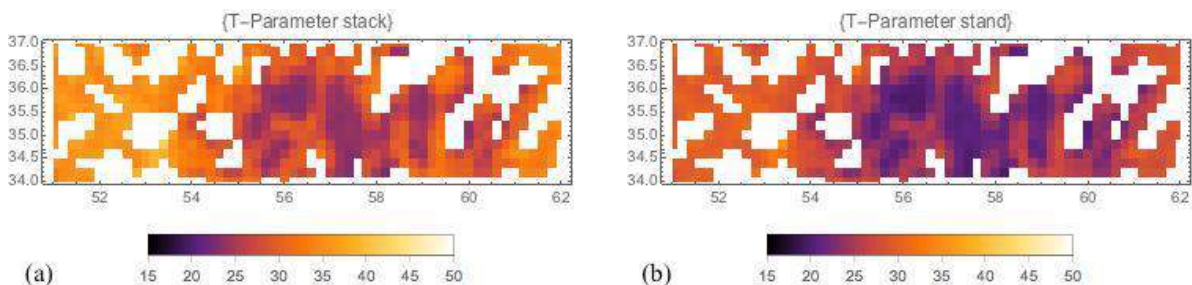
Region of normal bone tissue NO2

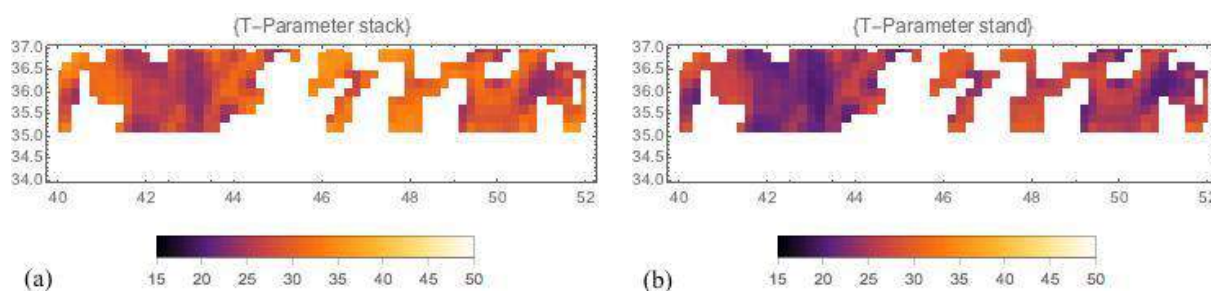figure 8.9 determined T-parameter plot from the SAXS measurements on the normal bone tissue sample 2 for both models: (a) stack of cards model; (b) Porod analysis; the x-axis and y-axis belong to the measured positions in millimetres, T-parameter values in units of Å

8.2.2 ρ-parameter

The evaluated ρ-parameters of the normal tissue samples showed some parts, where a reduction in the degree of orientation was present. This reduction occurred mainly in the cortical bone area of both normal tissue samples. In normal tissue sample 2 this observation was even more obvious than in normal tissue 1 (see

figure 8.10). The average values of the degree of orientation of the collagen fibrils were 0.35 (SD: 0.17) for normal bone tissue 1 and 0.27 (SD: 0.14) for the normal bone tissue 2 in average. Also the amount of isotropic points is, especially in normal bone tissue specimen 2, very high. Since the T-parameters where in these areas still constant, this could be a result of other bone mechanisms like healing mechanisms including the formation of new bone after an injury etc.
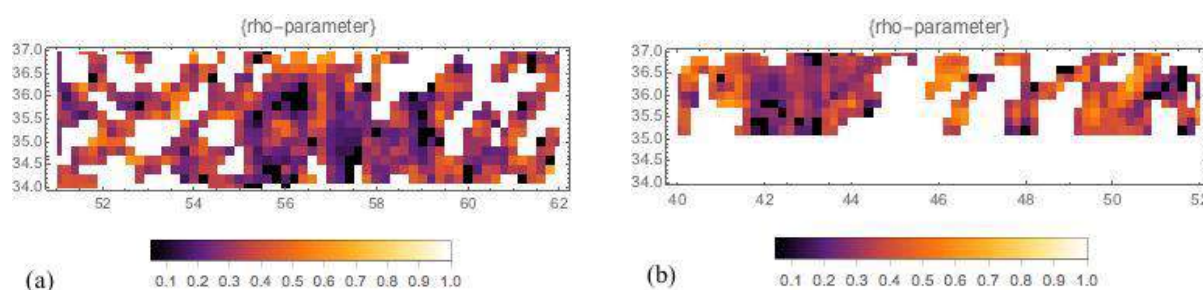
Region of normal bone tissue NO1 and NO2
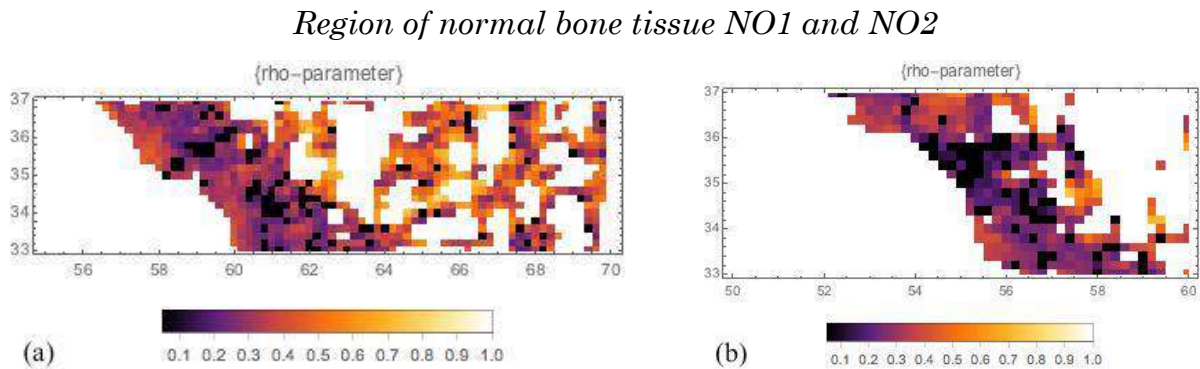
figure 8.10 determined degree of orientation plot from the SAXS measurements on the normal bone tissue samples 1 (left) and 2 (right); the x-axis and y-axis belong to the measured positions in millimetres,

8.3 Results crossing healthy and tumorous bone tissue samples
8.3.1 T-parameter

These bone tissue samples represented the transition between healthy and tumorous tissue. Prior, it was assumed, that this samples could contain areas, that are affected by the osteosarcoma cells. Measurements on the thickness of the mineral platelets showed that in some areas the thickness of the mineral platelets was obviously reduced. In figure 8.11 a clear reduction of the T-parameter on the right side can be assessed, differing remarkably from the rest of the measured part. The exact values are again shown in chapter 8.5, where one can also study the differences in thickness of the platelets between the different areas. In figure 8.12 a similar phenomenon can be observed in the bottom of the measured sample. Also there, areas of reduced thicknesses were found, but there the progress of the T-parameter was more cursive, which is shown in more detail in the chapter *discussion*.

Region of crossing bone tissue UG1
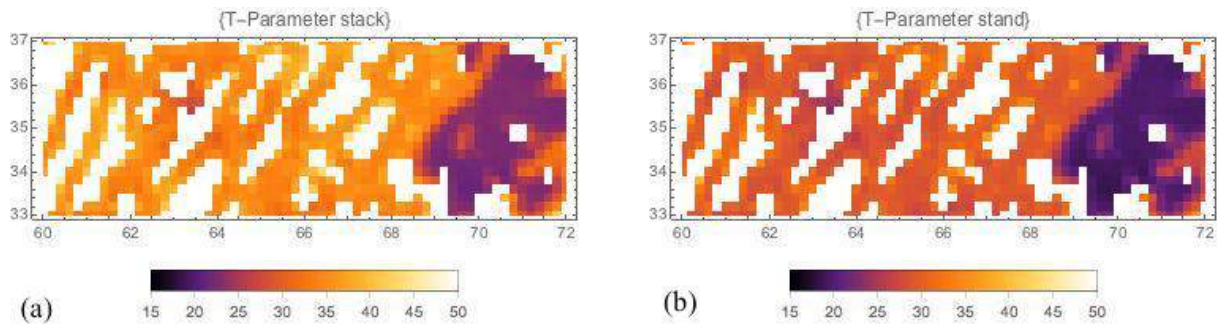
figure 8.11 determined T-parameter plot from the SAXS measurements on the crossing sample 1 for both models: (a) stack of cards model; (b) Porod analysis; the x-axis and y-axis belong to the measured positions in millimetres, T-parameter values in units of Å

Region of crossing bone tissue UG1 bottom
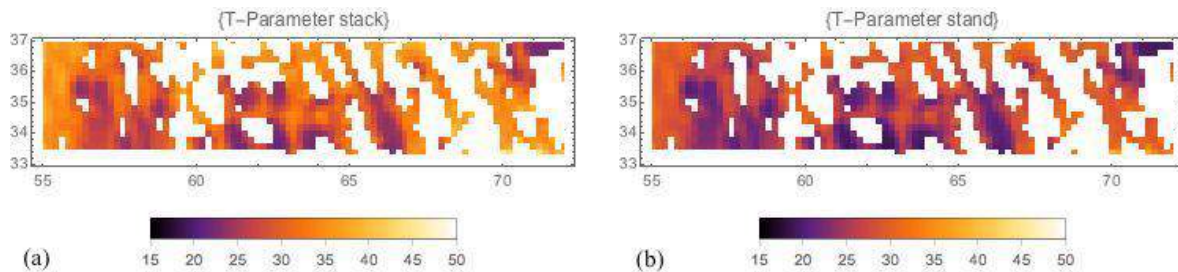
figure 8.12 determined T-parameter plot from the SAXS measurements on the bottom region of the crossing sample for both models: (a) stack of cards model; (b) Porod analysis; the x-axis and y-axis belong to the measured positions in millimetres, T-parameter values in units of Å

8.3.2 ρ-parameter

The obtained ρ-parameter of both measurements showed areas of a reduced degree of alignment of the mineral platelets and further distinct isotropic regions. Those parts were especially there present, where also the determined T-parameters were reduced. Especially in the crossing sample 1 (see figure 8.13a) a high part of isotropic points could be detected on the right hand side, besides lots of points with a reduced ρ-parameter.

Region of crossing bone tissue UG1 and UG1 bottom
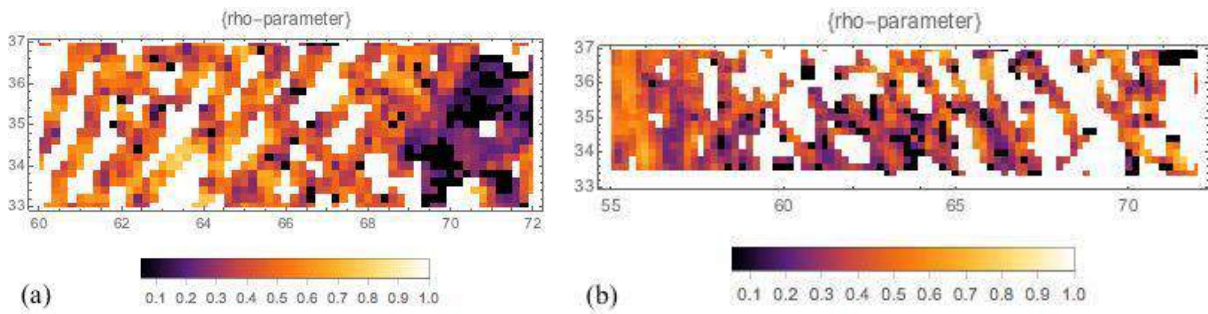
figure 8.13 determined degree of orientation plot from the SAXS measurements on the crossing tissue specimen 1 (left) and the bottom (right); the x-axis and y-axis belong to the measured positions in millimetres,

8.4 Results tumorous bone tissue samples

8.4.1 T-parameter

The results of the evaluation of the thickness of the mineral particles in the tumorous bone tissue samples delivered areas, where the T-parameter was remarkably reduced in comparison to that in the healthy bone tissue samples (compare to resection margin). The T-parameter, and therefore, the evaluated thicknesses where in a range of approximately 25 to 40Å in the stack of cards model and 20 to 35Å in the standard-model. The calculated, averaged thicknesses of the mineral platelets were for tumor tissue sample 1 (figure 8.14) 29.01 (SD: 3.5 Å) in stack of cards, and 24.88 (SD: 2.8 Å) in the standard model. For tumor tissue sample 3 (figure 8.14) the determined values were 30.26 Å (SD: 4.24 Å) and 25.81 Å (SD: 3.34 Å), respectively.

Region of tumorous bone tissue TU3

figure 8.14 determined T-parameter plot from the SAXS measurements on the tumorous bone tissue 3 for both models: (a) stack of cards model; (b) Porod analysis; the x-axis and y-axis belong to the measured positions in millimetres, T-parameter values in units of Å

figure 8.15 determined T-parameter plot from the SAXS measurements on the tumorous bone tissue 1 for both models: (a) stack of cards model; (b) Porod analysis; the x-axis and y-axis belong to the measured positions in millimetres, T-parameter values in units of Å

8.4.2 ρ-parameter

Even further, the degree of alignment of the mineral platelets in these samples was reduced in comparison to the healthy tissue samples. This phenomenon could, again, be observed in especially those areas where also the T-parameter was reduced. The found averaged values had been 0.35 (SD: 0.14) for tumor tissue sample 1 (figure 8.16b) and 0.31 (SD: 0.13) for tumor tissue sample 3(figure 8.16a).

Region of tumorous bone tissue TU3 and TU1

figure 8.16 determined degree of orientation plot from the SAXS measurements on the tumorous bone tissue samples 1 (right) and 3 (left); the x-axis and y-axis belong to the measured positions in millimeters

8.5 Summarized SAXS results and additional obtained parameters

In this chapter, the obtained values for the T- and ρ-parameter of all measured samples are listed, on the one hand to get a good overview and, on the other hand, to directly compare them. Figure 8.17 shows the evaluated T-parameters for both applied models, figure 8.18 the corresponding, determined degree of orientation of the platelets. Further, the obtained values are listed in table 8.1. It has to be mentioned that these values in the figures and the table represent

the calculated mean values of the whole sample including the standard deviation.
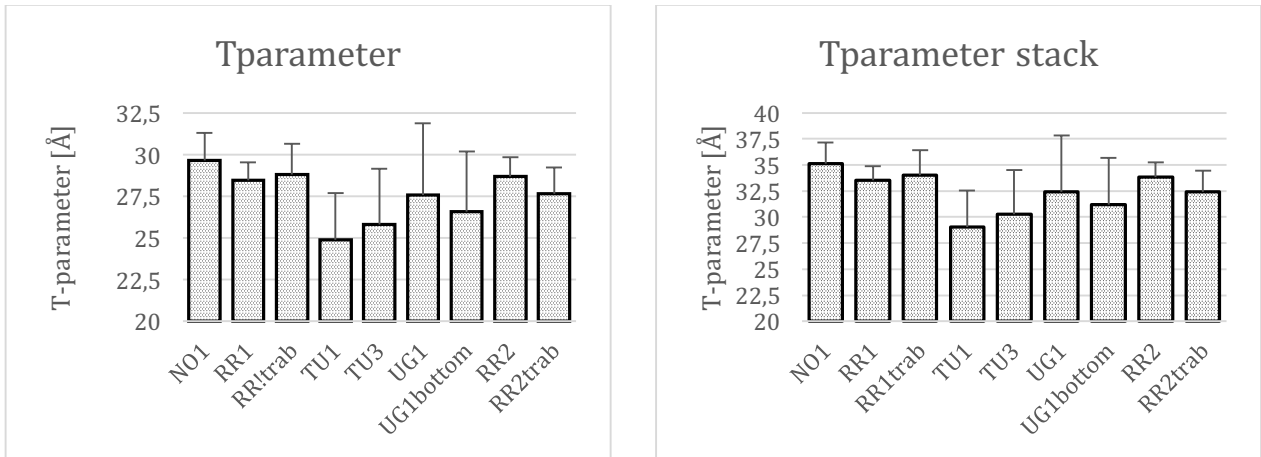
figure 8.17 plots of the calculated T-parameters in units of Angstrom for both models and all specimen; plotted values display the mean values including the standard deviation
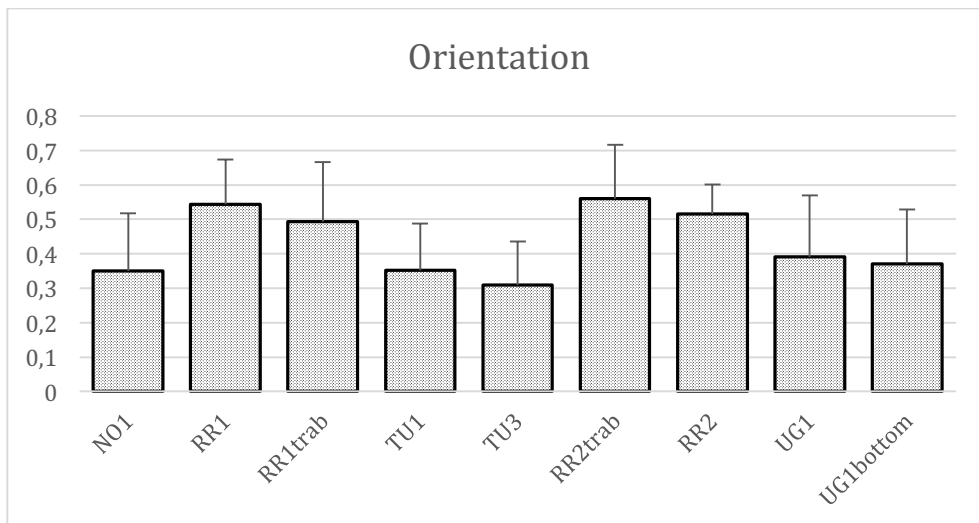
figure 8.18 plot of the calculated degree of orientation for all specimen; plotted values display the mean values including the standard deviation

Sample	T-parameter [Å]	SD [Å]	T-parameter stack [Å]	SD [Å]	Degree of orientation	SD [Å]
NO1	29.65	1.652	35.102	2.085	0.35	0.168
NO2	29.275	1.389	34.689	1.738	0.266	0.143
RR1	28.446	1.094	33.525	1.359	0.544	0.129
RR2	28,701	1.148	33.844	1.425	0.516	0.087
RR1trab	28.791	1.866	34.002	2.436	0.493	0.174
RR2trab	27.653	1.591	32.441	2.018	0.559	0.157
TU1	24.882	2.799	29.003	3.496	0.352	0.136
TU3	25.808	3.341	30.261	4.239	0.309	0.126
UG1	27.557	4.337	32.405	5.413	0.391	0.178
UG1bottom	26.573	3.601	31.199	4.484	0.371	0,158

table 8.1 evaluated T-parameter for both models and all samples: The T-parameter calculated by the Porod analysis and the T-parameter determined by the stack of cards model

Further, also the α and β parameter from the stack of cards model have been evaluated. The α parameter "controls the damping of the oscillations and, therefore, provides an indication of the relative extent of the ordering" (Gourrier et al., 2010, p. 1388), whilst the β parameter "describes the degree of spatial correlation between successive plates, separated by an average distance $d = T \frac{2\pi}{\beta}$ " (Gourrier et al., 2010, p. 1388). As it can be seen in table 8.2 these two parameters are reduced in the tumorous tissue parts. Furthermore a significant difference between normal and cancer bone parts can be suggested, since the standard deviation in the osteosarcoma specimen is partly higher than in the healthy bone samples. To get a further glance on the distributions and differences of these parameters over the bone areas, two graphics are listed in figure 8.19 and 8.20.

Sample	alpha	alpha SD	beta	beta SD
NO1	2.058	0.197	2.016	0.112
NO2	2.123	0.129	2.006	0.077
RR1	1.844	0.077	1.834	0.097
RR2	1.948	0.062	1.833	0.049
RR1trab	1.889	0.197	1.877	0.126
RR2trab	1.816	0.127	1.814	0.068
TU1	1.639	0.141	1.646	0.154
TU3	1.725	0.210	1.733	0.187
UG1	1.947	0.332	1.837	0.237
UG1bottom	1.854	0.229	1.775	0.195

table 8.2 evaluated α and β parameter for all specimen including the standard deviation (SD)
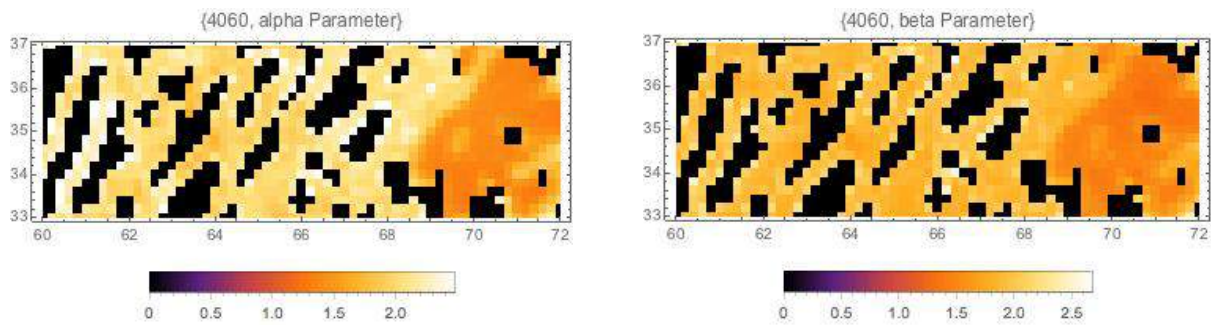
figure 8.19 plots of the α and β parameter in a region where both, tumorous and healthy bone tissue are occurring (crossing tissue specimen 1)
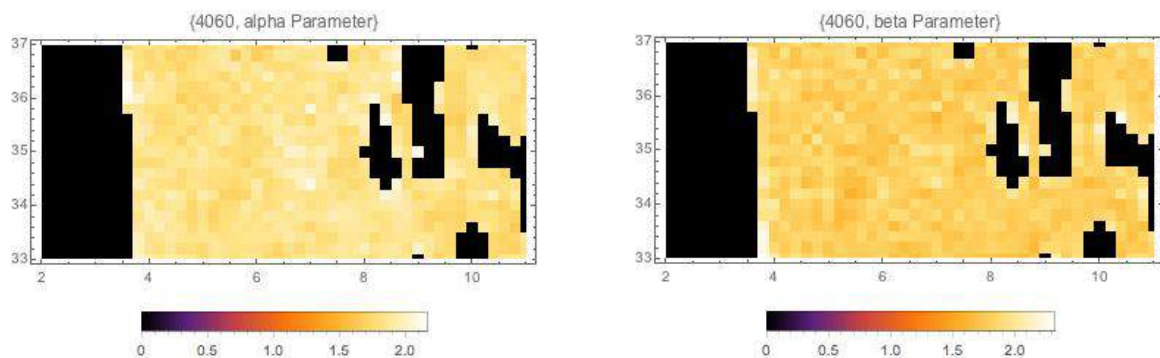
figure 8.20 plots of the α and β parameter in a region where only healthy bone is occurring (resection margin)

9. Results of the qBEI measurements on the bone samples

In this section the obtained backscattered electron images and the evaluation of the calculated calcium and bone mineral fraction values are presented. It has to be mentioned, even if the applied method is called *quantitative* backscattered electron imaging, it still can't be seen completely as such. If the grey values of the reference

samples are not completely stable and are varying to a small extent, this has in the further evaluation process a serious impact on the wt% calcium and the mineral volume fraction values. Further, also the threshold for the background has to be defined, which is another source for the distortion of the obtained values. Even further, the grey values of hydroxyapatite and osteoid were extrapolated, since such samples were not available. Nevertheless, it is still a good method to, at least, determine the tumorous parts, which is necessary to complement the SAXS measurements. Additionally, it still gives a glance on the differences of the mineral densities and wt% calcium values in the healthy and cancer areas, but the focus should not be laid on the values itself.

In the first step, backscattered images of the whole samples were made. Further, it was tried to fit these overall pictures to the regions, which were measured during the SAXS experiments, so that both areas match to make it comparable. Besides the calculation of the overall mineral volume fraction of the pictured samples, also regions of interests (ROIs) were analyzed. This was done because of two reasons. First, the grey values of the bone areas are distorted considerably less, because these ROIs contain only a minimum of other artefacts like the surrounding PMMA or any unintended contaminants in the embedding material. Second, through that it was possible to determine the wt% calcium of tumorous and surrounding healthy bone tissue parts separately.

The notation in the pictured figures was chosen in such way, that sample_*tu* refers to the tumorous bone tissue region of the sample, whilst sample_*norm* refers to regions where nothing but healthy bone tissue was present.

9.1 Backscattered electron images

In this section the most important obtained backscattered electron images are shown. On the one hand the overall images of the samples are presented, and on the other hand also the most interesting ROIs are shown to get an overview of what was made in the course of these experiments. It can be clearly seen for instance in figure 9.1 in the left upper image, which represents the crossing tissue sample, that the right area is affected by the osteosarcoma. Other tested samples, like the tumor samples, showed the same results.
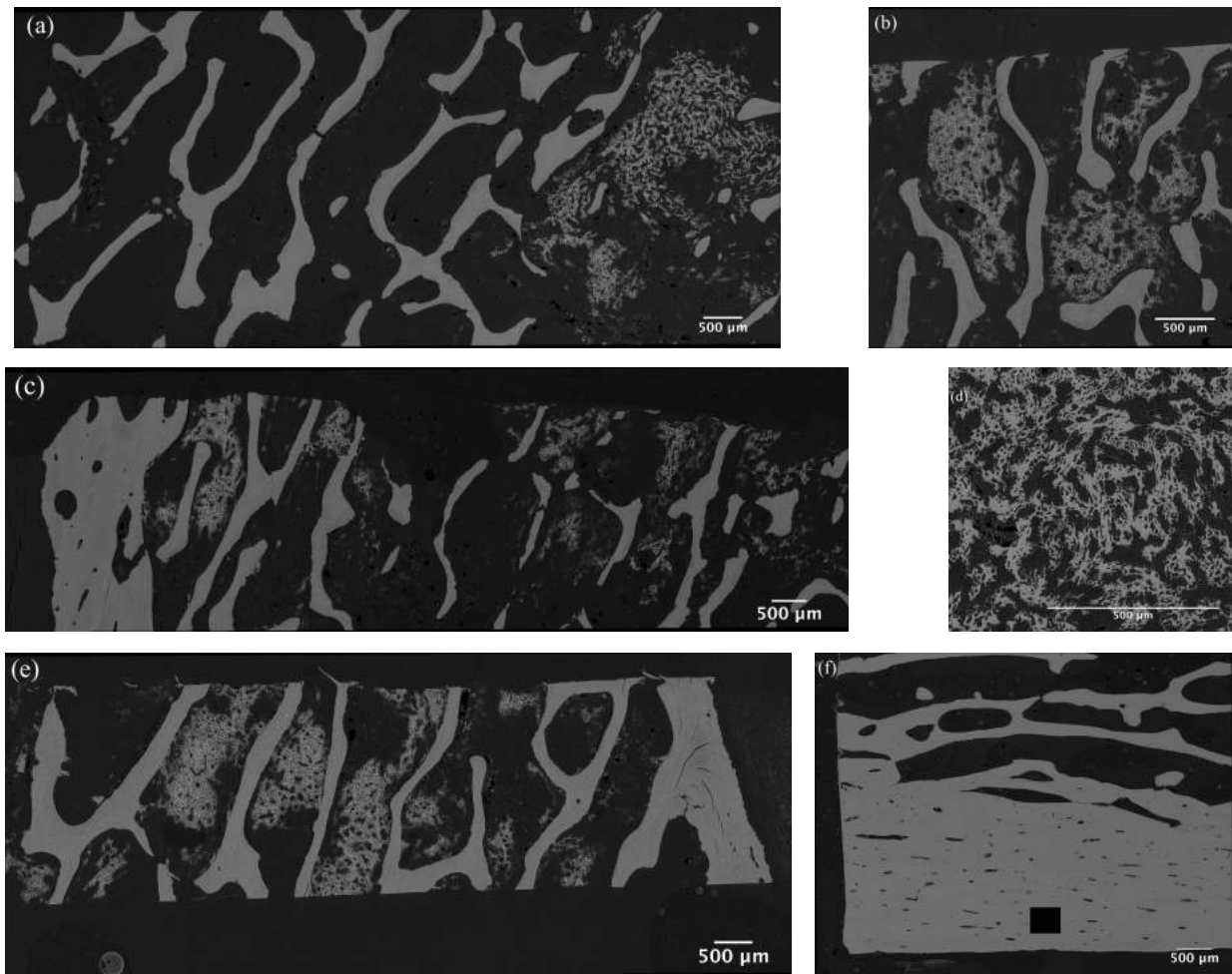
figure 9.1 obtained backscattered electron images for chosen bone samples and ROIs: (a) crossing sample UG1; (b) tumorous bone tissue sample TU3; (c) crossing tissue bottom UG1 bottom; (d) ROI tumorous bone tissue; (e) tumorous bone tissue sample TU1; (f) resection margin RR1, the black rectangle occurred due to a stitching failure and couldn't be corrected

9.2 Determined calcium and mineral volume fraction values

All values listed in this chapter were calculated by the applied methods described in chapter 7.2 and formula 7.1. Considering the backscattered images of the overall sample region, the highest calcium content (in wt%), including the mean and the peak value, were measured in the normal bone tissue sample, with about 24 and 24.5 wt%, respectively. The corresponding mineral volume fraction ϕ was determined to be about 40%.

The measured parts of the resection margin sample were for different bone areas (cortical and trabecular parts) nearly identical, with the mean and the peak calcium value ranging from 22.38 to 22.83 wt%. This resulted in an overall mineral volume fraction of about 37%.

The measurements of the overall tumorous bone tissue samples showed also mineral volume fraction values in the range of the resection margin samples, which was in numbers 35.31 and 37.86%. Differences can be seen in the peak wt% calcium value, which is higher in the tumorous parts. Also the difference between mean and peak value is higher, with about 1.3%, in the samples, where the cancer is present, compared to the healthy tissue samples (NO1: 0.52%; RR: 0.01%-0.23%). Thus, this indicates a broader distribution of measured calcium values in the tumorous areas.

Finally, the values of the crossing tissue sample were evaluated. There decreases in all values in comparison to all other samples were observed. Further, the difference between the two measured calcium values (mean and peak) was again in the range of the normal bone tissue and resection margin sample. All obtained values are summarized in table 9.1.

Sample	Ca_mean[wt%]	Ca_peak[wt%]	ϕ[%]
NO1	24.03	24.55	40.27
RR1	22.83	22.82	37.32
RR2	22.76	22.53	37.14
RR1trab	22.38	22.38	36.24
TU1	22.98	23.25	37.68
TU3	21.98	23.21	35.31
UG1	20.96	20.62	32.99
UG1bottom	17.12	17.41	25.04

table 9.1 obtained wt% calcium (mean and peak) and total mineral volume fraction values for all measured samples (over the whole specimen)

In the next step of procedure, the wt% calcium and mineral volume fraction values of the regions of interests where determined. The obtained results are outlined in table 9.2.

In comparison to the overall measured bone area, the normal bone tissue part shows now higher values of mean wt% calcium and of total mineralization, with 24.84% and 42.33% respectively. Still, the difference between the mean and the peak value is in the same range as before in the overall measurement.

The changes in cortical parts of the resection margin were insignificantly small (mean wt% calcium +0.01%), the values of the trabecular area were slightly reduced to a wt% calcium content of 22.09% and an overall mineral content of 35.55%. This result for the cortical bone area is absolutely reasonable, since in the overall backscattered image there were almost no artefacts which could influence the signal of the bone matrix. Through that, the differences between the whole area and the region of interest are almost nil.

Through the step of concentrating now on regions of interests, it is possible to observe cancer tissue parts and the surrounding healthy bone tissue separately. In all of these samples, represented by the two tumor tissue specimen and the crossing tissue part, the areas, where only the osteosarcoma was present, showed the same phenomenon: The mean calcium value was even higher than in the resection margin samples with values of 24 to 24.5%. Thus, this resulted in a total degree of mineralization of 40.3 to 41.8%. Even further, The difference between the peak and the mean calcium content noteworthy higher, ranging between 2.4% and even 3%. Apart from that, the surrounding normal bone regions in the osteosarcoma samples showed decreased calcium values and through that also a decreased total mineral volume fraction, when comparing it to the healthy bone tissue specimen. All of these measured values are shown in table 9.2.

Sample	Ca_mean[wt%]	Ca_peak[wt%]	ϕ[%]
NO1_norm	24.84	25.53	42.33
RR1_norm	22.84	22.82	37.34
RR1trab_norm	22.09	22.38	35.55
TU1_tu	24.63	27.64	41.79
TU1_norm	22.9	23.25	37.47
TU3_tu	24.23	26.64	40.76
TU3_norm	20.98	21.48	33.02
UG1_tu	24.07	26.58	40.36
UG1_norm	20.45	20.16	31.86
UG1bottom_tu	19.92	22.46	30.72
UG1bottom_norm	18.02	18.83	26.81

table 9.2 obtained wt% calcium (mean and peak) and total mineral volume fractions for all measured ROIs; ROIs were split up in healthy and tumorous bone tissue areas

9.2.1 Correction of the T-parameter

Through the fact that the T-parameter in both applied models was computed by the assumption that the mineral volume fraction is equal to 50% in the bone specimen, those values have to be corrected after the determination of the total mineral volume fraction.

This can be done by the so-called W-parameter, which is defined as (Zizak et al., 2003)

$$W = \frac{T}{2(1-\phi)} \qquad\qquad (9.1)$$

Since the obtained values for the mineral volume fraction are afflicted with some determination error through the calculation errors in the course of the grey value evaluation, the values of the W-parameter have to be used with caution. The obtained values can be seen in table 9.3 and figure 9.2.
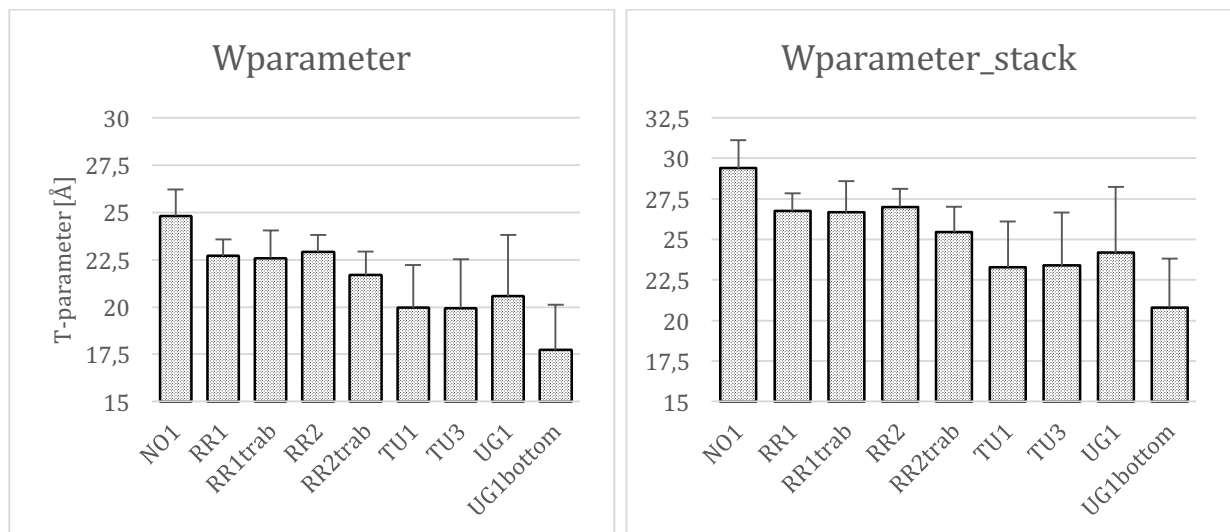
figure 9.2 Diagramm of the most important calculated W-parameter for both models (standard and stack of cards), which correct the mineral platelet thickness by considering the total mineral volume fraction;

Sample	W-parameter [Å]	SD [Å]	W-parameter stack [Å]	SD [Å]
NO1	24.82	1.38	29.38	1.75
RR1	22.69	0.87	26.74	1.08
RR1trab	22.58	1.46	26.66	1.91
RR2	22.89	0.92	26.99	1.14
RR2trab	21.89	1.25	25.45	1.58
TU1	19.96	2.24	23.29	2.81
TU3	19.95	2.58	23.39	3.28
UG1	20.56	3.23	24.18	4.04
UG1bottom	17.72	2.40	20.81	2.99

table 9.3 most relevant calculated W-parameter of the samples for both models (standard and stack of cards

IV. Discussion

10.1 Comparison SAXS and qBEI results

When comparing the obtained tumorous regions of the quantitative backscattered electron images to the SAXS plots, it can clearly be seen, that the (through the SAXS measurements) assumed osteosarcoma parts fit perfectly to the tumorous areas determined by the backscattered electron images. Through that it can be ensured, that the analyzed areas can be distinguished in healthy and cancer bone tissue parts. In figure 10.1 one comparison between the SAXS plot from the crossing tissue sample and the corresponding backscattered electron image can be seen. The area on the right side of the qBEI image shows a typical bone matrix formed by osteosarcoma cells. This area can now be seen in the SAXS plot differing significantly from the healthy bone regions (here in form of decreased mineral platelet thicknesses). Further, it can be stated, that in all measured bone samples, the tumorous areas of SAXS and qBEI match.
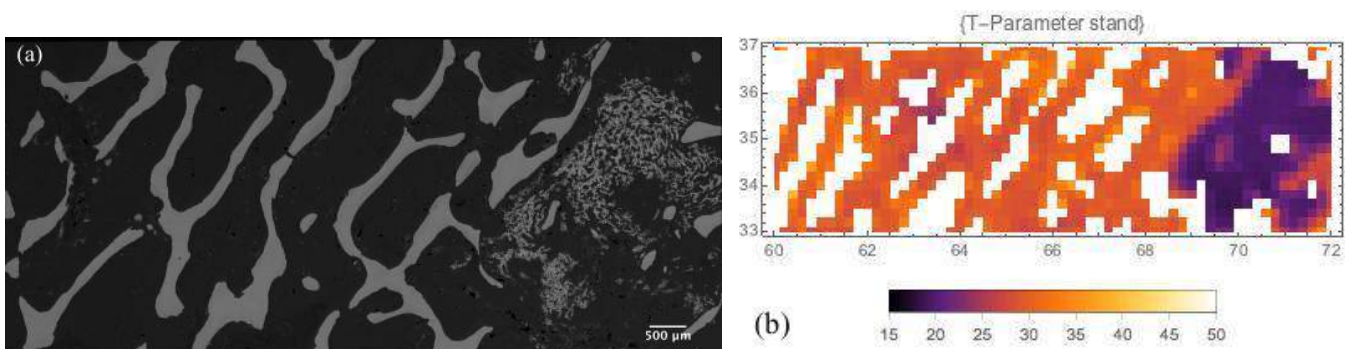
figure 10.1 comparison between (a) qBEI image and (b) SAXS plot: the corresponding tumorous regions can be clearly seen in both figures, here for the crossing tissue specimen 1

10.2 Bone mineral density and characterization of the type of osteosarcoma

The calculated values, although taking in account that the applied method is not quantitative, for the mean wt% calcium amount and the mineral volume fraction can still be used at least to point out the differences between healthy and tumorous bone tissue. The first finding, as it can be seen in table 9.1, is, that the overall mineral volume fractions in the tumor samples and the crossing sample are compared to the resection margin only slightly reduced. The overall mineral density in the normal bone region was the highest with about 40%. In a healthy

human body, the bone mineral density is assumed to be around 50%. Since this young man was bedridden for almost a year, it is quite plausible that also in the normal, healthy parts, the bone mineral density is reduced due to degradation mechanisms in the bone. Another possibility for the reduced bone mineral density is the fact that the applied chemotherapy can lead to a degradation of the bone matrix and to osteoporosis in the concerned bone regions (Pirker-Fruhauf, Friesenbichler, Urban, Obermayer-Pietsch, & Leithner, 2012). Further, it was prior expected, that the mineral volume fraction is even more reduced in the tumorous areas due to the malfunctions of the osteosarcoma, which can be seen for instance in the overall mineral volume fraction measurement of the tumor tissue sample TU3 and the crossing tissue sample in table 9.1.

 The second finding is, that the normal bone tissue parts, that are surrounding the osteosarcoma areas in the tumor samples, showed a noticeable mineral reduction in comparison to the normal bone tissue and a slight reduction as compared to the resection margin, which can be seen in table 9.2. One possibility for that, could be the result of a typical mechanism in osteosarcoma: various processes of the cancer cells, like the reduction of osteoprotegerin and the overexpression of RANKL, lead to a misbalanced state between osteoclasts and osteoblasts, and therefore to the destruction and degradation of healthy bone tissue. This degradation of the normal bone areas induced by the osteosarcoma could also explain the measured lower mineral content in those areas due to the lack of normal osteoblasts, which should form and mineralize new bone, but this is only one possible explanation for that observed phenomenon, amongst others.

The third observation was, that the mineral volume fraction in the tumorous areas formed by the osteosarcoma were elevated compared to the healthy bone parts which are surrounding these areas (the peak calcium values differed by up to 5 wt%), which is in complete contrast to what was expected before. Further, they showed even a higher mineralization degree than the resection margin and almost the same as the normal bone tissue sample. When analyzing the structure of the formed immature bone matrix (see figure 10.2), notable differences to a normal bone structure can be detected. The tumor areas showed areas with high amounts of pores together with areas of a more compact bone matrix. The larger differences between the mean and the peak wt% calcium value in the tumorous regions

compared to normal bone regions indicate a broader distribution of the degrees of mineralization, i.e. a higher heterogeneity.
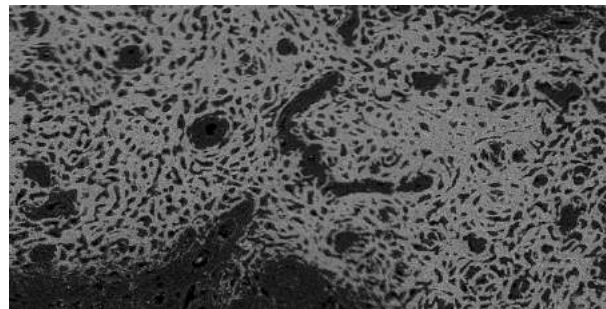
figure 10.2 region of interest: immature bone matrix formed by the osteosarcoma; image obtained via qBEI

Comparing these results to the observations Hofstaetter et al. made, it is likely, that the present samples were affected from a sclerosing osteosarcoma. In the alluded investigation almost the same differences and visual characteristics like higher wt% calcium values in the tumorous regions, and differences in the range of 5 wt% between the different bone areas could be detected. Also a broader distribution of calcium values in the tumorous regions was observed in both investigations. A short extract of the results is listed in figure 10.3 (Hofstaetter et al., 2013, p. 411). The conclusion about the presence of a sclerosing osteosarcoma is supported by histological data from the Medical University of Graz.

BMDD variables	TU	TB	Diff. TU-TB (%)	YoRef (n=54)	TU vs YoRef SD-score [Percentiles]	TB vs YoRef SD-score [Percentiles]
CaMean [wt% Ca]	25.54	21.56	18.5	20.95 (0.57)	+8	+1
CaPeak [wt% Ca]	27.38	22.36	22.5	21.66 (0.52)	+11	+1.3
CaWidth [Δwt% Ca]	3.64	2.60	40	3.47 [3.12;3.64]	[~80%]	[~2%]
CaLow [%]	8.22	5.34	53.9	6.14 [4.90;7.99]	[~75%]	[~50%]
CaHigh [%]	79.08	0.79	9910	0.89 [0.43;1.47]	[>100%]	[~50%]
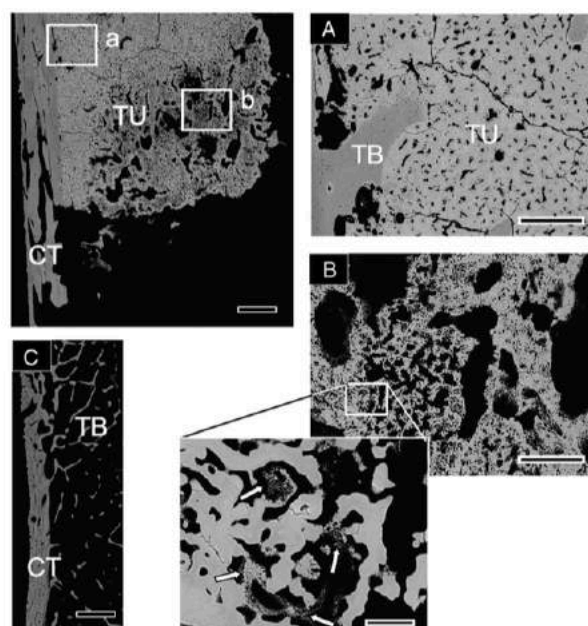
figure 10.3 results and backscattered electron images from the research of Hofstaetter et al.

Finally, it has to be said, that the focus should not be laid on the grey values itself, but on the qualitative differences BEI is able to show between tumorous and healthy bone tissue areas. Further, the values of the UG1_bottom sample should be not overinterpreted, since they were extremely reduced to the other samples of the same type. This could be the result of an error in combination with the reference samples, e.g. that some parts were not exactly in the same plane since it was a very large specimen. Nevertheless, the differences in wt% calcium between tumorous and the surrounding healthy bone tissue are the same as in the other samples and can still be considered relevant. One possible explanation of the higher mineralization values of the normal bone tissue compared to the resection margin could be through the ongoing bone healing mechanisms and through that the production of new bone, in this area, as described before.

10.3 Differences of the mineral thickness in healthy and tumorous bone tissue

The determined thicknesses of the mineral platelets were, for both applied models, almost normally distributed for the resection margin (including cortical and trabecular areas) and the normal bone tissue samples, see figures 10.4 and 10.5. Further, when studying the histograms, it can be seen that the distribution covers only a small range of thickness values, indicating almost a constant thickness of the mineral platelets over the whole measured area. In comparison to that, the distributions of the T-parameter in the crossing tissue sample and the tumorous tissue samples are differently distributed. In the crossing bone specimen two clear peaks in the histogram can be detected (see figure 10.5a-b), indicating healthy and tumorous bone tissue. In the osteosarcoma specimen (see figure 10.5c-f), the thickness of the mineral platelets is clearly reduced; additionally, the distributions are broader than in the resection margin or the normal bone tissue specimen in figure 10.4. When studying again table 8.1, a reduction of the overall mean T-parameter of about 5 Å can be observed in the samples that are affected by the osteosarcoma. This reduction is detected for the whole sample, which means, that the particle thicknesses in the tumorous regions are even more reduced. This can be seen especially in the two peaks in crossing tissue sample histogram (see figure 10.5a-b), where the peak of the T-parameter in the cancer parts was at

approximately 20 and 22.5 Å for the standard and the stack of cards model in comparison to the peaks of healthy bone tissue parts being at approximately 30 and 35 Å, respectively. Further, when studying figure 10.6 it can be seen, that the values of the healthy bone tissue parts only vary within a very small range, with 50% of the data points ranging in a span of only about 2.5 Å, whilst the tumorous sample show a wider spread of values (about 6-8 Å) due to the influences of the osteosarcoma. The second insight figure 10.6 gives, is the information about the lowest measured values for the T-parameter. The lowest measured values in the healthy bone regions were about 30 Å for the stack of cards model and about 25.5 Å for the standard model. In comparison to that, the lowest measured thicknesses in the osteosarcoma samples were about 23 for stack of cards, and approximately 19 in the standard model.

Also after the correction of the T-parameter, meaning the calculation of the W-parameter, the thicknesses of the mineral platelets of course reduce, but still the differences between the two areas (healthy and osteosarcoma bone tissue) stay the same. To sum up, these observations delivered a clear reduction of the thickness of the mineral platelets in osteosarcoma for both applied models of approximately up to 10 Å. Since the evaluated histograms for all measured resection margin and normal bone tissue regions were distributed the same, identical way, only one of each region (resection margin cortical and trabecular, and one normal bone tissue region) is shown in the figures.

The differences between the values of the two models is simply by the different calculations of the models itself. Nevertheless, they both deliver reasonable values and in both models the differences between normal and tumorous bone tissue are the same.
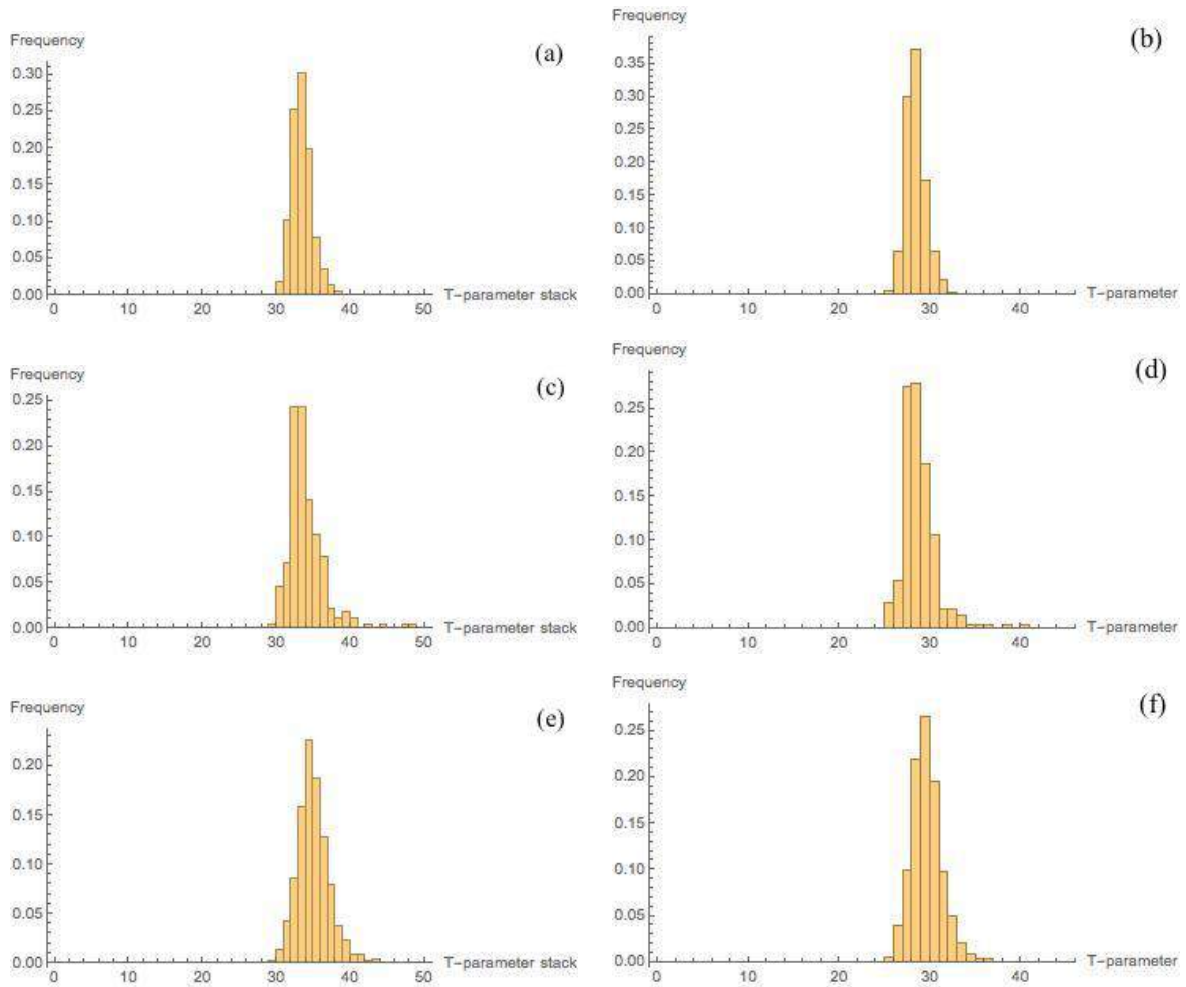
figure 10.4 obtained histograms for the T-parameter for both models: (a) resection margin cortical stack of cards, (b) resection margin cortical standard, (c) resection margin trabecular stack of cards, (d) resection margin trabecular standard, (e) normal bone tissue stack of cards, (f) normal bone tissue standard
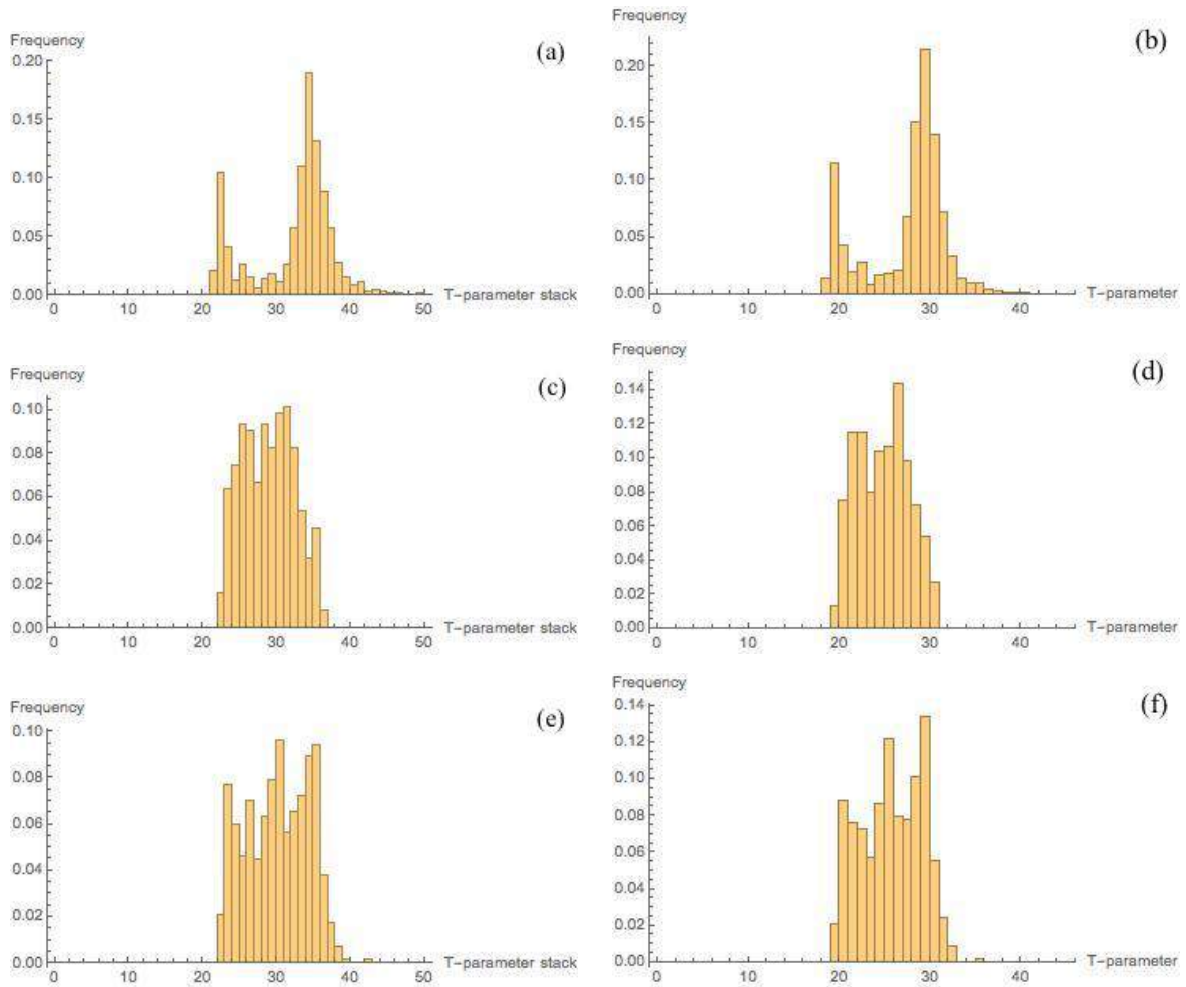
figure 10.5 obtained histograms for the T-parameter for both models: (a) crossing tissue sample stack of cards, (b) crossing tissue sample standard, (c) tumor tissue sample 1 stack of cards, (d) tumor tissue sample 1 standard, (e) tumor tissue sample 3 stack of cards, (f) tumor tissue sample 3 standard
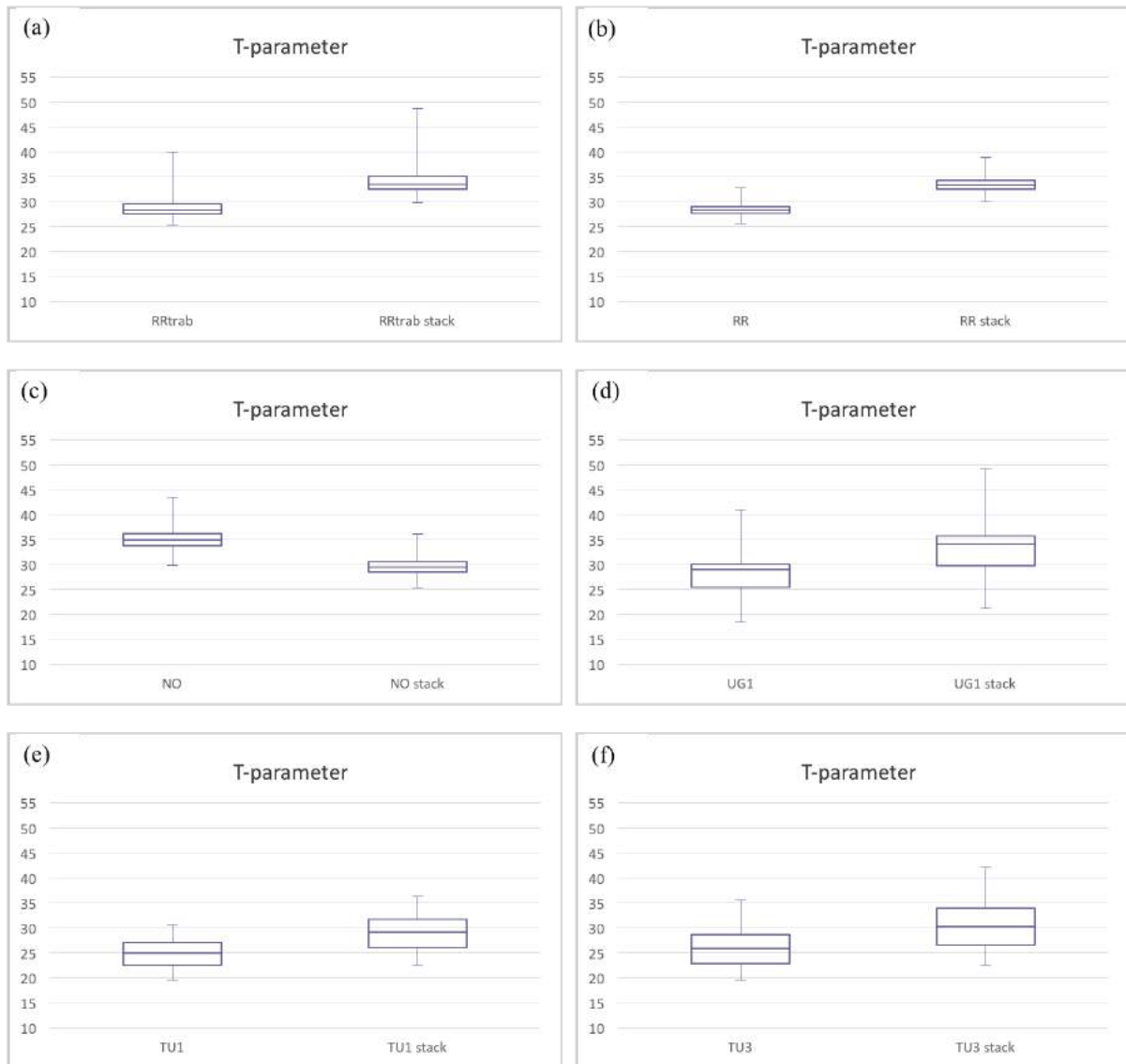
figure 10.6 obtained box-plots for the investigated samples of the T-parameter for both applied models; (a) resection margin sample RR1 trabecular bone area, (b) resection margin RR1 cortical bone area, (c) normal bone tissue NO1, (d) crossing tissue sample UG1, (e) tumorous bone tissue TU1, (f) tumorous bone tissue TU3

10.4 Differences in the degree of orientation of the collagen fibrils in healthy and tumorous bone tissue

Also for the degree of orientation of the collagen fibrils, significant differences between healthy and tumorous bone tissue were observed. According to Zizak et. al. the value of the ρ-parameter in healthy bone should be of about 0.5 (Zizak et al., 2003, p. 214).

The cortical parts of the resection margin showed a normal distribution of the obtained values with a peak between 0.5 and 0.6 for the overall degree of orientation. The histogram of the investigated trabecular bone area of the resection margin sample 1 shows at first glance a high peak of isotropic points. Since the

density of points, where bone tissue is present, is lower in comparison to e.g. the cortical bone areas, and all points, which are set to be almost zero, are summarized to the isotropic points, this effect is multiplied. Nevertheless, when studying the histogram, we can still detect a normal distribution around the peak value of 0.5. The determined mean values of the ρ-parameter were 0.54 and 0.51 for the cortical parts and 0.49 and 0.56 for the trabecular parts, respectively. Thus these determined results correlate well with the findings of Zizak et.al.

Comparing the values from the healthy tissues to those, where the osteosarcoma was present (UG1, TU1, TU3), the following can be detected: The overall degree of orientation is shifted towards a peak value of 0.3 to 0.4, with the determined mean values of 0.35 and 0.31 for the tumor samples and 0.39 for the crossing tissue sample (see figure 10.7a-f and table 8.1). In addition to that, a high amount of isotropic points was determined, which were mainly located in the cancer areas, which can be seen also in the plots in the chapter *results*. In these plots, it can be also seen, that in the parts, where only tumorous bone tissue was present, the degree of orientation only reaches values in the range of 0.2 or even below, which is clearly reduced compared to healthy bone tissue parts. A fact, which underlines this, is that the mean values are calculated for the whole samples, meaning that also the values for normal bone tissue parts are included. As a consequence, , if one would only measure the tumorous parts, these value should then be even more reduced to those of the whole specimen.

When studying figure 10.8, it can be seen, that on the one hand 75% of the obtained data points in the resection margin areas are above a ρ-parameter value of about 0.4 to 0.5 (RR1: 0.474, RR2: 0.461, RR1trab: 0.413, RR2trab: 0.474). On the other hand, in the specimen where tumorous bone tissue parts were present, 75% of the data points were only above 0.25 (TU1: 0.272, TU3: 0.231, UG1: 0.28, UG1bottom: 0.285) and further, seen from the other side, 75% were below a value of 0.5 (TU1: 0.44, TU3: 0.38, UG1: 0.52, UG1bottom: 0.479). Thus, it can be clearly said, that in the tumorous regions a clear reduction of the degree of orientation of the collagen fibrils was detected.

The obtained values of the degree of orientation in the normal tissue sample may have to be treated separately. They were extremely reduced, but still the T-parameter was equal to those measured in the resection margin. Even further, the

qBEI analysis of this specimen showed no hints of any cancer parts. Thus, this reduction of the orientation could be the result of other injuries and/or bone healing mechanisms.

Furthermore, through the obtained structure of the osteosarcoma, or to be more precise, the formed immature bone matrix, the measured values for the degree of orientation have to be handled with some care. As mentioned before, the tumorous bone matrices had pores with diameters in the range of 10 to 100 μm. Through the fact that the provided machine setup can't resolve such a structure (min. beam size is 200 μm), it could be that a reduction of the overall orientation is measured, whilst still local parts of the bone matrices show a local orientation and trough that a higher ρ-parameter. Further, this could also have an influence on the T-parameter, since Dr. Tilman Gruenewald reported, that the first measurements on the mineral platelet thicknesses at the ESRF showed not that high drop between normal and tumorous bone tissue. More information on this assumption can be expected from the overall results of the measurements that were made at the ESRF by Dr. Gruenewald (parts of the results can be seen in the appendix). The provided machine setup there allows a higher resolution of the samples, which results in a more precise description of the degree of orientation.

Nevertheless, the obtained results strongly hint at a reduction in the alignment of the collagen fibrils in osteosarcoma and these experiments correlate well with a recent study carried out by He et.al. and observed the influence on the mineral platelets in the case of bone metastasis through a breast cancer in mice. They observed the same phenomena, which are decreased thickness of the mineral platelets and a reduction in the degree of orientation, with similar values as obtained in this thesis for a sclerosing osteosarcoma in the human bone (He et al., 2017, pp. 2-6).

The results in this thesis give new insights in the devastating mechanisms of osteosarcomas: Due to the lack of orientation and the reduced thickness of the mineral particles, also the mechanical properties of bone be negatively affected. Thus, these findings, especially the observation of the decrease in the overall orientation, can help to improve the interplay between the field of biomaterials/biomechanics and the field of cancer research, or can also give new

suggestions in the field of the development of treatment routines like e.g. chemotherapies.
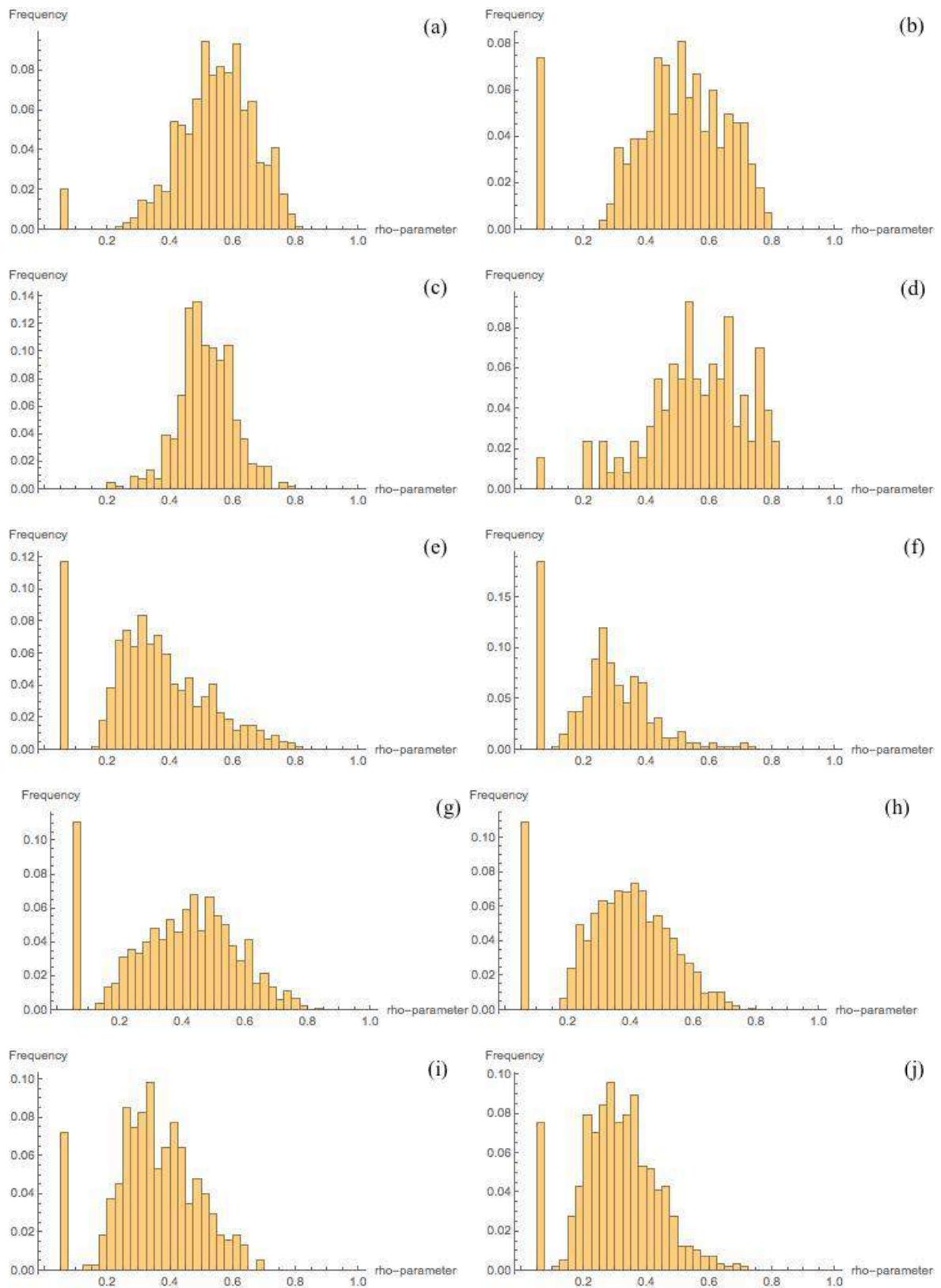
figure 10.7 obtained histograms for the degree of orientation: (a) resection margin 1 cortical, (b) resection margin 2 cortical, (c) resection margin 1 trabecular, (d) resection margin 2 trabecular, (e) normal bone tissue 1, (f) normal bone tissue 2, (g) crossing sample 1, (h) crossing sample bottom, (i) tumorous tissue 1, (j) tumorous tissue 3
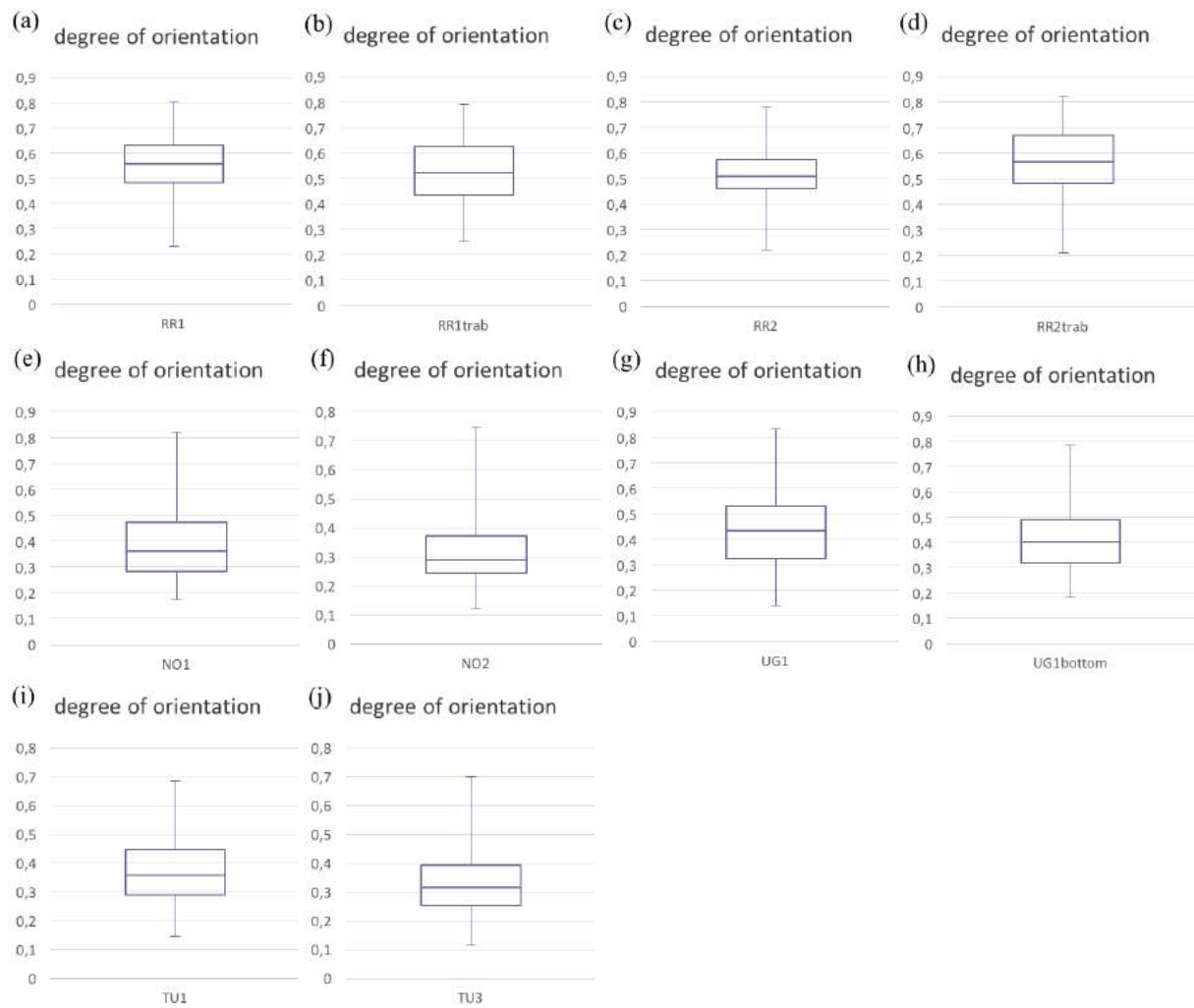
figure 10.8 obtained box-plots for the investigated samples of the degree of orientation of the collagen fibrils; (a) resection margin RR1 cortical bone, (b) resection margin RR1 trabecular bone, (c) resection margin RR2 cortical bone, (d) resection margin RR2 trabecular bone, (e) normal bone tissue sample NO1, (f) normal bone tissue sample NO2, (g) crossing tissue sample UG1, (h) crossing tissue sample UG1 bottom area, (i) tumorous bone tissue sample TU1, (j) tumorous bone tissue sample TU3

V. Conclusion

The aim of this thesis was to determine the influence of an osteosarcoma on the nanostructure of bone, i.e. the thickness of the mineral platelets and the degree of orientation of the collagen fibrils. This was achieved by small angle x-ray scattering. All available bone samples, which were kindly provided by the Medical University of Graz, were scanned with this technique. For complementary information, the bone samples were additionally investigated by the method of quantitative backscattered electron imaging (BEI). In this way, the location of the tumorous areas could be confirmed. Further, also the degree of mineralization was determined in the course of these measurements. Although this can't be seen as a quantitative analysis, it still shows at least the differences between the two types of bone areas (healthy and tumorous). Through that, it was also possible to determine the type of osteosarcoma in the present case, which turned out to be a sclerosing osteosarcoma. To sum up, in this thesis the following points were shown:

- The reduction of the mineral platelet thicknesses in the tumorous bone tissue areas compared to the healthy parts
- The decrease in the degree of orientation of the collagen fibrils in the cancer parts compared to the normal bone tissue parts
- The presence of a sclerosing osteosarcoma, implied through a higher degree of mineralization in the cancer tissue compared to the surrounding normal bone tissue

Still, there are procedures, that can be optimized to obtain even more precise results. One thing would be the improvement of the measurement of the bone mineral density through BEI. In this thesis, a linear correlation between the grey values and the wt% calcium was assumed, based on the literature. Still, this could be tested by a third reference sample. In the course of this thesis, it was unfortunately not possible since aluminum didn't work out as a reference material, and other materials which would fit were not available at the time. Furthermore, the standardization could be made with osteoid and hydroxyapatite, but also here the problem was the access to those samples, or obtain a flat polished surface, respectively. Nevertheless, it was possible to detect the differences between normal and tumorous bone tissue very well with the given setup.

To sum up, through these observations it was possible to get new insights in the mineralization of osteosarcoma and the effect on surrounding bone. Still, there has to be a huge amount of research work to be done, to rudimentarily understand the full – and complex – mechanisms of cancer. Nevertheless, this was another step in the right direction to improve the knowledge of these malignant mechanisms, and hopefully this contributes to someday to at least enhance the possibilities of finding better treatment options.

VI. Appendix

A.1 Osteosarcoma

A.1.1 Aetiology

In the past two decades, major new insights in the mechanisms leading to osteosarcomas as well as their behaviour could be achieved. Still, the exact cell of origin from which this type of bone cancer arises is not known for sure. Two theories which origin osteosarcomas could have are nowadays supported: either mesenchymal stem cells (MSC), or committed osteoblast precursors could be possibilities as the cells of origin (Mutsaers & Walkley, 2014, p. 56). It is important to know, that the (bone-marrow-resident) mesenchymal stem cells have the ability to give raise to chondrocytes, adipocytes and osteoblasts (Nombela-Arrieta, Ritz, & Silberstein, 2011, p. 126). The knowledge about which cells are initiating the tumours could improve the therapies, which could then be more personalized, and the life of many people, which is up to now unfortunately not always possible (Mutsaers & Walkley, 2014, p. 56).

Up to now many different types of bone neoplasms are known and characterized like osteosarcoma, chondrosarcoma or Ewing's sarcoma. These three malignant tumours also make up almost 75% of all bone cancer affected patients (Damron, Ward, & Stewart, 2007). As already mentioned, scientists are eager to find the origin of these diseases. A possibility could be that all these different types of sarcoma are the result of mutations within the mesenchymal stem cells (Xiao, Mohseny, Hogendoorn, & Cleton-Jansen, 2013, p. 4), as they give rise to the osteoblasts (Mutsaers & Walkley, 2014, p. 59).

In contrast to that, another option is that the different bone tumours arise from mutations of the distinct cell populations. In the case of an osteosarcoma the origin could then be mutations in pre-osteoblasts. OS has a peak during childhood and adolescence, which are phases of rapid bone growth and rapid cell divisions, where both, mesenchymal stem cells and osteoblast precursors are involved. Thus, definite knowledge about the cell of origin can only be gained by further studies on human osteosarcoma samples (Mutsaers & Walkley, 2014, pp. 57-61).

A.1.1.1 Hypothesis of cancer stem cells

So far, nearly every form of cancer is reported in some cases to show resistance against the applied therapy or to return again after a complete remission. These facts led to the development of a cell model, the so-called cancer stem cell hypothesis, which is elucidated here.

Normal tissues in the human body are arising from diverse cell populations, from which they are also composed of. Therein, also the tissue stem cells are present. These cells have the ability to give rise to precursor cells, which are more differentiated, and able to self-renew. In the cancer stem cell hypothesis, a heterogeneous population of cells forms the tumour, which is made up of cells, that show different degrees of proliferation, differentiation and carcinogenicity. Further, also in this population a subpopulation of cells, which are referred to as cancer stem cells, exists. It is believed, that they possess also the ability to renew themselves and that they are the top of a hierarchical cell structure where the stem cells give rise to the diverse cancer and non-tumour genic cells. Hence, also in a hierarchical cell structure, the cancer stem cells can arise either from more differentiated cells (precursor cells) or normal tissue stem cells. The precursor cells may have received the stem cell functions through mutations. Consequently, the cell of origin has no influence on the cancer stem cell hypothesis (Dela Cruz, 2013, p. 1).

Osteosarcoma is an aggressive bone tumour, the 5-year survival rate lays between 50 and 65%. Further, the cancer metastasizes, the most frequent route is pulmonary into the lungs. About 15% of all osteosarcoma patients are affected by metastases, further in nearly 80% of all patients mircometastases are expected (Luu et al., 2005, p. 319), with a survival rate of under 20% (Dela Cruz, 2013, p. 4). Thus, finding and identifying cancer stem cells could mainly improve the survival rate of this disease, especially for those cases, where also metastases are occurring. Recent studies tried to investigate such cancer stem cells in various forms of malignant tumours, including osteosarcoma. In the research of Tirino et al., the glycoprotein CD133 was used in order to detect cells with stem cell-like properties (Tirino et al., 2008, p. 1). Before, CD133 was used successful in various studies, for example by identifying a cell subpopulation in the brain associated to be carcinogenic, which further showed stem cell properties in vitro (Singh et al., 2004,

pp. 396-397). It was tried to find stem cells in three different isolated osteosarcoma cell lines by the use of CD133 as a marker. As a result, in all cell lines CD133^{+} could be detected with an amount of 3-5% of all cells. The evaluated data and the fact that CD133^{+} only represented a small amount of all cells indicate that these could be cancer stem cells. (Tirino et al., 2008, pp. 2-3)

Although many breakthroughs in this field of research could be reached, it is still a controversial field. It is up to now not known if this model can be generalized for all types of cancer, or even within one type of malignant tumour for all patients.

A.2 ESRF Data

The experiments were carried out at the ESRF in Grenoble by Dr. Tilman Gruenewald, who also kindly provided his data for this thesis.

The investigations on the crossing tissue sample showed in the tumorous parts, which can be seen when studying figure A.3.1 and the corresponding color wheel, some local orientations of the formed immature bone matrix, but these alignments are varying a lot over the whole region, which is then resulting in the decreased orientation which was observed in this thesis. The normal, healthy bone parts showed again the expected high degree of orientation, which can also be seen in figure A.3.2 in the investigated resection margin sample. Thus, these first results confirm the detected changed degree of orientation of the collagen fibrils in the tumorous bone tissue regions. Still, more results on that would give much more and detailed information on the alignment of the fibrils in osteosarcoma, but the measured data from other tumorous regions were up to now unfortunately not available.
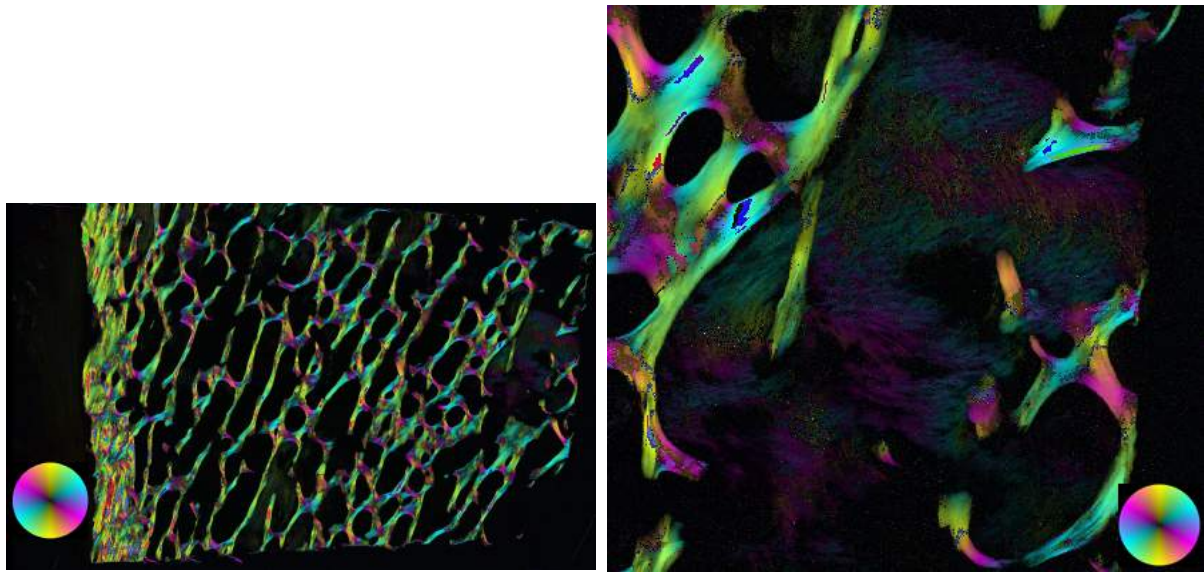
figure A.3.1 SAXS measurement on the crossing sample overall (left) and the tumorous region (right), plot of the degree of orientation
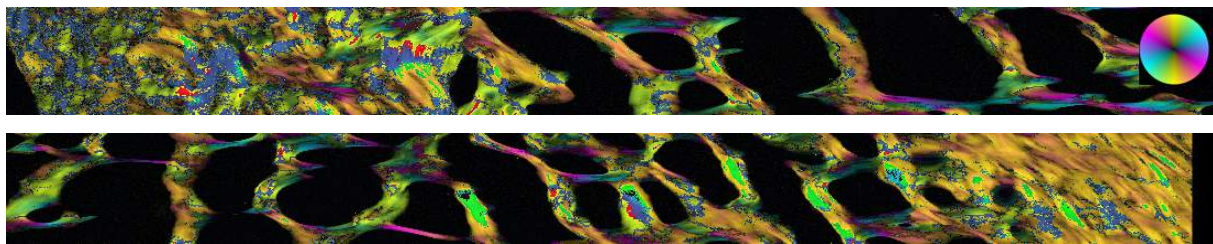
figure A.3.2 SAXS measurement on the resection margin sample, upper image: left sample part, lower image: right sample part; plot of the degree of orientation

A.3 Table of figures

A.4 Bibliography

Akiyama, T., Dass, C. R., & Choong, P. F. (2008). Novel therapeutic strategy for osteosarcoma targeting osteoclast differentiation, bone-resorbing activity, and apoptosis pathway. *Mol Cancer Ther, 7*(11), 3461-3469. doi:10.1158/1535-7163.MCT-08-0530

Avnet, S., Longhi, A., Salerno, M., Halleen, J. M., Perut, F., Granchi, D., . . . Baldini, N. (2008). Increased osteoclast activity is associated with aggressiveness of osteosarcoma. *Int J Oncol, 33*(6), 1231-1238.

Benayahu, D., Shur, I., Marom, R., Meller, I., & Issakov, J. (2001). Cellular and molecular properties associated with osteosarcoma cells. *J Cell Biochem, 84*(1), 108-114.

Branstetter, D., Rohrbach, K., Huang, L. Y., Soriano, R., Tometsko, M., Blake, M., . . . Dougall, W. C. (2015). RANK and RANK ligand expression in primary human osteosarcoma. *J Bone Oncol, 4*(3), 59-68. doi:10.1016/j.jbo.2015.06.002

Broadhead, M. L., Clark, J. C., Myers, D. E., Dass, C. R., & Choong, P. F. (2011). The molecular pathogenesis of osteosarcoma: a review. *Sarcoma, 2011*, 959248. doi:10.1155/2011/959248

Broadhead, M. L., Dass, C. R., & Choong, P. F. (2009). Cancer cell apoptotic pathways mediated by PEDF: prospects for therapy. *Trends Mol Med, 15*(10), 461-467. doi:10.1016/j.molmed.2009.08.003

Damron, T. A., Ward, W. G., & Stewart, A. (2007). Osteosarcoma, chondrosarcoma, and Ewing's sarcoma: National Cancer Data Base Report. *Clin Orthop Relat Res, 459*, 40-47. doi:10.1097/BLO.0b013e318059b8c9

Dela Cruz, F. S. (2013). Cancer stem cells in pediatric sarcomas. *Front Oncol, 3*, 168. doi:10.3389/fonc.2013.00168

Foley, J. M., Scholten, D. J., 2nd, Monks, N. R., Cherba, D., Monsma, D. J., Davidson, P., . . . Steensma, M. R. (2015). Anoikis-resistant subpopulations of human osteosarcoma display significant chemoresistance and are sensitive to targeted epigenetic therapies predicted by expression profiling. *J Transl Med, 13*, 110. doi:10.1186/s12967-015-0466-4

Franchi, A., Arganini, L., Baroni, G., Calzolari, A., Capanna, R., Campanacci, D., . . . Zampi, G. (1998). Expression of transforming growth factor beta isoforms in osteosarcoma variants: association of TGF beta 1 with high-grade osteosarcomas. *J Pathol, 185*(3), 284-289. doi:10.1002/(SICI)1096-9896(199807)185:3<284::AID-PATH94>3.0.CO;2-Z

Fratzl, P., Gupta, H. S., Paschalis, E. P., & Roschger, P. (2004). Structure and mechanical quality of the collagen-mineral nano-composite in bone. *Journal of Materials Chemistry, 14*(14), 2115-2123. doi:10.1039/b402005g

Fratzl, P., & Weinkamer, R. (2007). Nature's hierarchical materials. *Progress in Materials Science, 52*(8), 1263-1334. doi:10.1016/j.pmatsci.2007.06.001

Georgiadis, M., Muller, R., & Schneider, P. (2016). Techniques to assess bone ultrastructure organization: orientation and arrangement of mineralized collagen fibrils. *J R Soc Interface, 13*(119). doi:10.1098/rsif.2016.0088

Gourrier, A., Li, C. H., Siegel, S., Paris, O., Roschger, P., Klaushofer, K., & Fratzl, P. (2010). Scanning small-angle X-ray scattering analysis of the size and organization of the mineral nanoparticles in fluorotic bone using a stack of cards model. *Journal of Applied Crystallography, 43*, 1385-1392. doi:10.1107/S0021889810035090

Gruenewald, T. A., Ogier, A., Akbarzadeh, J., Meischel, M., Peterlik, H., Stanzl-Tschegg, S., . . . Lichtenegger, H. C. (2016). Reaction of bone nanostructure to a biodegrading Magnesium WZ21 implant - A scanning small-angle X-ray scattering time study. *Acta Biomaterialia, 31*, 448-457. doi:10.1016/j.actbio.2015.11.049

He, F., Chiou, A. E., Loh, H. C., Lynch, M., Seo, B. R., Song, Y. H., . . . Fischbach, C. (2017). Multiscale characterization of the mineral phase at skeletal sites of breast cancer metastasis. *Proc Natl Acad Sci U S A, 114*(40), 10542-10547. doi:10.1073/pnas.1708161114

Hofstaetter, J. G., Roschger, A., Puchner, S. E., Dominkus, M., Sulzbacher, I., Windhager, R., . . . Roschger, P. (2013). Altered matrix mineralization in a case of a sclerosing osteosarcoma. *Bone, 53*(2), 409-413. doi:10.1016/j.bone.2012.12.043

Jens Als-Nielsen, D. M. (2011). *Elements of modern X-ray physics*.

Kansara, M., & Thomas, D. M. (2007). Molecular pathogenesis of osteosarcoma. *DNA Cell Biol, 26*(1), 1-18. doi:10.1089/dna.2006.0505

Krinsley, D. H. (1998). *Backscattered scanning electron microscopy and image analysis of sediments and sedimentary rocks*: Cambridge.

Luu, H. H., Kang, Q., Park, J. K., Si, W., Luo, Q., Jiang, W., . . . He, T. C. (2005). An orthotopic model of human osteosarcoma growth and spontaneous pulmonary metastasis. *Clin Exp Metastasis, 22*(4), 319-329. doi:10.1007/s10585-005-0365-9

Mahlendorf, D. E., & Staege, M. S. (2013). Characterization of Ewing sarcoma associated cancer/testis antigens. *Cancer Biol Ther, 14*(3), 254-261. doi:10.4161/cbt.23298

Marina, N., Gebhardt, M., Teot, L., & Gorlick, R. (2004). Biology and therapeutic advances for pediatric osteosarcoma. *Oncologist, 9*(4), 422-441.

Mascarenhas, L., Siegel, S., Spector, L., Arndt, C., Femino, D., & Malogolowkin, M. (1998). Malignant bone tumors. *Cancer epidemiology in older adolescents and young adults, 15*.

Mottaghitalab, F., Hosseinkhani, H., Shokrgozar, M. A., Mao, C., Yang, M., & Farokhi, M. (2015). Silk as a potential candidate for bone tissue engineering. *J Control Release, 215*, 112-128. doi:10.1016/j.jconrel.2015.07.031

Mutsaers, A. J., & Walkley, C. R. (2014). Cells of origin in osteosarcoma: mesenchymal stem cells or osteoblast committed cells? *Bone, 62*, 56-63. doi:10.1016/j.bone.2014.02.003

Nikitovic, D., Kavasi, R. M., Berdiaki, A., Papachristou, D. J., Tsiaoussis, J., Spandidos, D. A., . . . Tzanakakis, G. N. (2016). Parathyroid hormone/parathyroid hormone-related peptide regulate osteosarcoma cell functions: Focus on the extracellular matrix (Review). *Oncol Rep, 36*(4), 1787-1792. doi:10.3892/or.2016.4986

Nombela-Arrieta, C., Ritz, J., & Silberstein, L. E. (2011). The elusive nature and function of mesenchymal stem cells. *Nat Rev Mol Cell Biol, 12*(2), 126-131. doi:10.1038/nrm3049

Olszta, M. J., Cheng, X. G., Jee, S. S., Kumar, R., Kim, Y. Y., Kaufman, M. J., . . . Gower, L. B. (2007). Bone structure and formation: A new perspective. *Materials Science & Engineering R-Reports, 58*(3-5), 77-116. doi:10.1016/j.mser.2007.05.001

Pabisch, S., Wagermaier, W., Zander, T., Li, C., & Fratzl, P. (2013). Imaging the nanostructure of bone and dentin through small- and wide-angle X-ray scattering. *Methods Enzymol, 532*, 391-413. doi:10.1016/B978-0-12-416617-2.00018-7

Parisuthiman, D., Mochida, Y., Duarte, W. R., & Yamauchi, M. (2005). Biglycan modulates osteoblast differentiation and matrix mineralization. *Journal of Bone and Mineral Research, 20*(10), 1878-1886. doi:10.1359/JBMR.050612

Pautke, C., Schieker, M., Tischer, T., Kolk, A., Neth, P., Mutschler, W., & Milz, S. (2004). Characterization of osteosarcoma cell lines MG-63, Saos-2 and U-2 OS in comparison to human osteoblasts. *Anticancer Res, 24*(6), 3743-3748.

Pirker-Fruhauf, U. M., Friesenbichler, J., Urban, E. C., Obermayer-Pietsch, B., & Leithner, A. (2012). Osteoporosis in children and young adults: a late effect after chemotherapy for bone sarcoma. *Clin Orthop Relat Res, 470*(10), 2874-2885. doi:10.1007/s11999-012-2448-7

Rajabalian, S., Hajializadeh, Z., Pooraboli, I., Jangi-Aghdam, H., & Badinloo, M. (2010). Establishment, characterization, and drug sensitivity of a new Ewing sarcoma cell line (SS-ES-1). *J Pediatr Hematol Oncol, 32*(8), e331-337. doi:10.1097/MPH.0b013e3181ee4d16

Reznikov, N., Chase, H., Brumfeld, V., Shahar, R., & Weiner, S. (2015). The 3D structure of the collagen fibril network in human trabecular bone: Relation to trabecular organization. *Bone, 71*, 189-195. doi:10.1016/j.bone.2014.10.017

Rho, J. Y., Kuhn-Spearing, L., & Zioupos, P. (1998). Mechanical properties and the hierarchical structure of bone. *Medical Engineering & Physics, 20*(2), 92-102. doi:Doi 10.1016/S1350-4533(98)00007-1

Roschger, P., Fratzl, P., Eschberger, J., & Klaushofer, K. (1998). Validation of quantitative backscattered electron imaging for the measurement of mineral density distribution in human bone biopsies. *Bone, 23*(4), 319-326. doi:http://doi.org/10.1016/S8756-3282(98)00112-4

Roschger, P., Grabner, B. M., Rinnerthaler, S., Tesch, W., Kneissel, M., Berzlanovich, A., . . . Fratzl, P. (2001). Structural Development of the Mineralized Tissue in the Human L4 Vertebral Body. *Journal of Structural Biology, 136*(2), 126-136. doi:http://dx.doi.org/10.1006/jsbi.2001.4427

Savage, S. A., & Mirabello, L. (2011). Using Epidemiology and Genomics to Understand Osteosarcoma Etiology. *Sarcoma, 2011*. doi:10.1155/2011/548151

Schnablegger, H., Singh, Yashveer. (2013). *The SAXS-Guide - Getting acquainted with the principles*: Anton Paar GmbH.

Schrof, S., Varga, P., Galvis, L., Raum, K., & Masic, A. (2014). 3D Raman mapping of the collagen fibril orientation in human osteonal lamellae. *J Struct Biol, 187*(3), 266-275. doi:10.1016/j.jsb.2014.07.001

Singh, S. K., Hawkins, C., Clarke, I. D., Squire, J. A., Bayani, J., Hide, T., . . . Dirks, P. B. (2004). Identification of human brain tumour initiating cells. *Nature, 432*(7015), 396-401. doi:10.1038/nature03128

Strauss, S. J., Ng, T., Mendoza-Naranjo, A., Whelan, J., & Sorensen, P. H. (2010). Understanding micrometastatic disease and Anoikis resistance in ewing family

of tumors and osteosarcoma. *Oncologist, 15*(6), 627-635. doi:10.1634/theoncologist.2010-0093

Ta, H. T., Dass, C. R., Choong, P. F., & Dunstan, D. E. (2009). Osteosarcoma treatment: state of the art. *Cancer Metastasis Rev, 28*(1-2), 247-263. doi:10.1007/s10555-009-9186-7

Tirino, V., Desiderio, V., d'Aquino, R., De Francesco, F., Pirozzi, G., Graziano, A., . . . Giordano, A. (2008). Detection and characterization of CD133+ cancer stem cells in human solid tumours. *PLoS One, 3*(10), e3469. doi:10.1371/journal.pone.0003469

Trinidad, E. M., & Gonzalez-Suarez, E. (2016). RANKL inhibitors for osteosarcoma treatment: hope and caution. *Ann Transl Med, 4*(24), 534. doi:10.21037/atm.2016.12.10

Varga, P., Pacureanu, A., Langer, M., Suhonen, H., Hesse, B., Grimal, Q., . . . Peyrin, F. (2013). Investigation of the three-dimensional orientation of mineralized collagen fibrils in human lamellar bone using synchrotron X-ray phase nano-tomography. *Acta Biomaterialia, 9*(9), 8118-8127. doi:10.1016/j.actbio.2013.05.015

von Eisenhart-Rothe, R., Toepfer, A., Salzmann, M., Schauwecker, J., Gollwitzer, H., & Rechl, H. (2011). [Primary malignant bone tumors]. *Orthopade, 40*(12), 1121-1142. doi:10.1007/s00132-011-1866-7

Wang, Y., & Petrova, V. (2012). Scanning Electron Microscopy *Nanotechnology Research Methods for Foods and Bioproducts* (pp. 103-126): Wiley-Blackwell.

Xiao, W., Mohseny, A. B., Hogendoorn, P. C., & Cleton-Jansen, A. M. (2013). Mesenchymal stem cell transformation and sarcoma genesis. *Clin Sarcoma Res, 3*(1), 10. doi:10.1186/2045-3329-3-10

Yabluchanskiy, A., Ma, Y., Iyer, R. P., Hall, M. E., & Lindsey, M. L. (2013). Matrix metalloproteinase-9: Many shades of function in cardiovascular disease. *Physiology (Bethesda), 28*(6), 391-403. doi:10.1152/physiol.00029.2013

Yan, G. N., Lv, Y. F., & Guo, Q. N. (2016). Advances in osteosarcoma stem cell research and opportunities for novel therapeutic targets. *Cancer Lett, 370*(2), 268-274. doi:10.1016/j.canlet.2015.11.003

Yang, R., Hoang, B. H., Kubo, T., Kawano, H., Chou, A., Sowers, R., . . . Gorlick, R. (2007). Over-expression of parathyroid hormone Type 1 receptor confers an aggressive phenotype in osteosarcoma. *Int J Cancer, 121*(5), 943-954. doi:10.1002/ijc.22749

Zizak, I., Roschger, P., Paris, O., Misof, B. M., Berzlanovich, A., Bernstorff, S., . . . Fratzl, P. (2003). Characteristics of mineral particles in the human bone/cartilage interface. *Journal of Structural Biology, 141*(3), 208-217. doi:10.1016/S1047-8477(02)00635-4